Fractal spike dynamics and neuronal coupling in the primate visual system

Brandon Munn[1,2*], Natalie Zeater[2,3*], Alexander N. Pietersen[2,3], Samuel G. Solomon[4,5], Soon Keen Cheong[2,3], Paul R. Martin[2,3,4] and Pulin Gong[1,2]

*Equal Contribution

[1]University of Sydney, School of Physics, New South Wales 2006, Australia

[2]University of Sydney, Australian Research Council Centre of Excellence for Integrative Brain Function, New South Wales 2006, Australia

[3]University of Sydney, Save Sight Institute, Eye Hospital Campus, New South Wales 2001, Australia

[4]University of Sydney, Discipline of Physiology, New South Wales 2006, Australia

[5] University College London, Department of Experimental Psychology, London WC1P 0AH, UK

Corresponding authors:

Paul R Martin, Save Sight Institute, University of Sydney Eye Hospital Campus, 8 Macquarie St NSW 2001, Australia (prmartin@sydney.edu.au)

Pulin Gong, School of Physics, University of Sydney, NSW 2006, Australia (pulin.gong@sydney.edu.au)

33 pages; 9 figures; 1 table

Conflict of interests: None.

Key Points (max 150 words/5 dot-points)

- We measured fractal (self-similar) fluctuations in ongoing spiking activity in subcortical (lateral geniculate nucleus, LGN) and cortical (area MT) visual areas in anaesthetised marmosets.

- Cells in the evolutionary ancient koniocellular LGN pathway and in area MT show high-amplitude fractal fluctuations, whereas evolutionary newer parvocellular and magnocellular LGN cells do not.

- Spiking activity in koniocellular cells and MT cells shows substantial correlation to the local population activity, whereas activity in parvocellular and magnocellular cells is less correlated with local activity.

- We develop a model consisting of a fractal process and a global rate modulation which can reproduce and explain the fundamental relation between fractal fluctuations and population coupling in LGN and MT.

- The model provides a unified account of apparently disparate aspects of neural spiking activity and can improve our understanding of information processing in evolutionary ancient and modern visual pathways.

Abstract (max 250 words)

The brain represents and processes information through patterns of spiking activity, which is influenced by local and wide-scale brain circuits as well as intrinsic neural dynamics. Whether these influences have independent or linked effects on spiking activity is however not known. Here we measured spiking activity in two visual centres, the lateral geniculate nucleus (LGN) and cortical area MT, in marmoset monkeys. By combining the Fano-factor time curve, power spectral analysis, and

2

rescaled range analysis, we reveal inherent fractal fluctuations of spiking activity in LGN and MT. We found that the evolutionary ancient koniocellular (K) pathway in LGN and area MT exhibit strong fractal fluctuations at short (< 1 s) timescales. Parvocellular (P) and magnocellular (M) LGN cells show weaker fractal fluctuations at longer (multi-second) timescales. In both LGN and MT, the amplitude and timescale of fractal fluctuations can explain short– and long-timescale spiking dynamics. We further show differential neuronal coupling of LGN and MT cells to local population spiking activity. The population coupling is intrinsically linked to fractal fluctuations: neurons showing stronger fluctuations are more strongly correlated to the local population activity. To understand this relationship, we modelled spiking activity using a fractal inhomogeneous Poisson process with dynamic rate which is the product of an intrinsic stochastic fractal rate and a global modulatory gain. Our model explains the intrinsic links between neuronal spike rate and population coupling in LGN and MT, and establishes a unified account of dynamic spiking properties in afferent visual pathways.

Introduction

Neural circuits represent and process information through the temporal and spatial patterns of their spikes. Neuronal spike patterns are highly variable, and display substantial diversity across neurons, during both maintained[1] activity and evoked responses (Softky and Koch, 1993; Churchland et al., 2011). Understanding these spike patterns is therefore important for understanding how the brain processes information.

Spike rates in neurones in the early visual system are known to display fractal (self-similar) property, as observed in retina, lateral geniculate nucleus (LGN), and primary visual cortex (V1) of cats (Baddeley et al., 1997; Teich et al., 1997), and monkey inferotemporal cortex (Baddeley et al., 1997). Other works show that, at least in primary visual cortex (V1; Okun et al., 2015) and motor cortex (Kells et al., 2019), neuronal spike rate is variably correlated with the pooled spike rate of other neurons (population coupling) and that (at least for the motor cortex) population coupling is related to motor coding. Here we show in measurements from the primate visual system that fractal

---

[1] Spiking activity in absence of patterned visual stimulation. Sometimes referred to as spontaneous activity.

3

dynamics and population coupling are linked, and we develop an explanatory unifying model. The model shows how fractal fluctuations can explain differences in spiking dynamics and population coupling between distinct functional cell types in both areas.

In neurons throughout the visual pathway, the variance in spike rate usually exceeds the mean rate, and rarely falls below it. That is, neurons display super-Poisson variability (Tolhurst and Thompson, 1981; Goris et al., 2014). Classical Poisson models of neuronal variability (Dayan and Abbott, 2003) cannot account for super-Poisson variability. Evoked responses in V1 (Ecker et al., 2014; Goris et al., 2014) and maintained activity in primary auditory cortex (Lowen and Teich, 1996) and LGN (Teich et al., 1997) can nevertheless be captured by an inhomogeneous Poisson process (a Poisson process with a dynamic rate). These models show that spike rates of single neurons, and correlations between pairs of neurons, are consistent with presence of global gain changes that fluctuate over time (Ecker et al., 2014; Goris et al., 2014). However, these models are incapable of explaining both the fractal variability of spike activity and the observed variability in population coupling. Thus, it is not known whether and how the phenomena of spike variability, population coupling, and correlated variability are related.

The primate lateral geniculate nucleus (LGN) comprises three parallel visual processing streams. These streams are anatomically identified as the parvocellular (P), magnocellular (M) and koniocellular (K) layers of the LGN. Functionally, the three streams are specialised for transmission of different visual signals from retina to cortex. The P-cells serve high-acuity vision at high image contrasts, and red-green colour vision, whereas M-cells serve motion perception and spatial vision at low image contrast (reviewed by Nassi and Callaway, 2009; Lee et al., 2010). The K pathway is considered evolutionarily more primitive than the P and M pathways, having more diffuse and widspread connections with visual cortices and subcortical visual centers (reviewed by Jones, 2001). The K-cells show heterogeneous receptive field properties including blue-yellow colour selectivity (Martin et al., 1997; Tailby et al., 2008a), orientation selectivity (Xu et al., 2002; Cheong et al., 2013) and suppressed-by-contrast characteristic (Tailby et al., 2007; Zeater et al., 2015). The K-cells also differ from P-cells and M-cells as they show synchronisation of activity at timescales typically seen in primary visual cortex, and have spike rates entrained to cortical EEG (Cheong et al., 2011). Here, we examine spiking dynamics in these parallel subcortical visual pathways in the LGN, and in the motion-processing visual cortical area MT. Spike trains in both LGN and MT were measured in absence of patterned visual stimulation (i.e. uniform illumination) to make the datasets comparable

4

across subcortical and cortical recordings. We show that spike rate fluctuations in both LGN and MT can be characterized as fractal, indicating the existence of long-range temporal correlations. We demonstrate that pair-wise correlations in spike rate are related to the nature of the long-range correlations within the spike pattern, most prominently in LGN K-cells and in area MT, and that neurons with larger spike rate variance (Fano-factor) are more strongly coupled to population activity.

We synthesise our findings by reproducing the spike dynamics with a stochastic fractal inhomogeneous Poisson process. The dynamic rate of this process is the product of fractal Brownian motion (a fractal stochastic signal) and a global modulatory gain with white noise dynamics. Using this model, we can quantitatively reproduce both the fractal variability and population coupling within the LGN and area MT. We discover an intrinsic link between these two apparently distinct empirical findings through the Hurst exponent (the Hurst exponent is a measure of fractal variability). We find that a larger Hurst exponent leads to both a larger Fano-factor (Teich et al., 1997) and to greater population coupling (Okun et al., 2015). Together, these results establish a unified account of spike rate variability across subcortical and cortical areas.

Methods

Ethical approval

Procedures were approved by the institutional (University of Melbourne and University of Sydney) Animal Experimentation and Ethics Committee, and conform to the Society for Neuroscience and NHMRC policies on the use of animals in neuroscience research, as well as with the reporting guidelines of *The Journal of Physiology* (Grundy, 2015).

Animal preparation and cell recordings

Male marmosets (*Callithrix jacchus*, n=5) were obtained from the Australian National Health and Medical Research Council (NHMRC) combined breeding facility. Animals were housed in family groups and given *ad libitum* access to food and water. Recordings were made separately from the LGN of three marmosets (cases MA024, MA025, and MY146; typically 1200 s per recording epoch) and from area MT of two marmosets (cases MA027 and MY144; typically 300 s per recording epoch); 27 cells were isolated from MA024 in three recordings, three cells were isolated from MA025 in one

5

recording, 19 cells were isolated from MY146 in six recordings, and 15 cells were isolated from the two MT recordings.

Details of surgical preparation were given previously (Solomon et al., 2011; McDonald et al., 2014). Each animal was initially anaesthetised with an intramuscular injection of 12 mg kg^{-1} Alfaxan (Jurox, NSW, Australia) and 3 mg kg^{-1} Diazepam (Roche, NSW, Australia). Anaesthesia and analgesia were maintained by intravenous infusion of sufentanil citrate (6–30 μg kg^{-1} h^{-1}) and inspired 70:30 mixture of N_2O and carbogen (5% CO_2, 95% O_2). Dominance of low frequencies (1–5 Hz) in the electro-encephalogram (EEG) recording and absence of EEG or electrocardiogram changes under intermittent noxious stimulus (tail pinch) were taken as the chief signs of an adequate level of anaesthesia. We found that low anaesthetic dose rates in the range cited above were always very effective during the first 24 h of recordings. Thereafter, drifts towards higher frequencies (5–10 Hz) in the EEG record were counteracted by increasing the rate of venous infusion or the concentration of anaesthetic.

Extracellular recordings were made using a Neuronexus (16×2 recording surfaces, surface separation 50 μm, shank separation 500 μm) silicon array probe (for LGN recordings) or multielectrode ("Utah") arrays (10 x 10 electrodes, 1.5 mm length, electrode spacing 400 μm, Blackrock Microsystems) for MT recordings. Details of recording procedures were given previously (Solomon et al., 2011; McDonald et al., 2014; Zeater et al., 2015). Recordings from MT and LGN were made independently, but experimental conditions were as far as possible kept identical for the two sets of recordings. Signals from each contact point were amplified, bandpass-filtered (0.3–5 kHz), and digitized at a rate of 24 kHz using an RZ2 real-time processor (Tucker-Davis Technologies). Single-cell and multi-unit activity were classified off-line using commercial (Plexon) and in-house software written in MATLAB. As described previously (Solomon et al., 2014) voltage waveforms of single cells were discriminated by principal component analysis of amplified voltage signals. Isolated cells were retained for analysis if evoked responses to visual stimuli was at least 5 spikes sec^{-1} above the maintained activity. At least 1 minute settle time was allowed between measurements of evoked responses and the long-epoch measure of maintained activity. After each set of measurements in LGN the recording probe was advanced by 500 μm, and after 30 minutes settle time the stimulus set and maintained activity measures were repeated.

The typical duration of a recording session was 48–72 h. At the end of the experiment, the animal was euthanised via intravenous infusion of 300–600 mg kg^{-1} sodium pentobarbitone

6

(Lethobarb, Virbac). The animal was perfused transcardially with 0.9% saline followed by 4% paraformaldehyde in 0.1M phosphate buffer (PB, pH 7.4) and the 10% glycerol in PB. The brain was removed and placed in 20% glycerol for 24–72 hours, then coronally sectioned at 50 μm on a freezing microtome for histological electrode track reconstruction.

Visual stimulus and cell classification

Visual stimuli were generated using custom software (EXPO, Peter Lennie) and presented to the animal via a front-silvered mirror on a CRT monitor (Sony G520, refresh rate 100 Hz, viewing distance 114 cm, mean luminance 45–55 cd m^{-2}). Visual stimuli comprised temporal square-wave intensity and/or chromaticity modulation of a spatially uniform circular field (pulse, duration 200 ms; 100 repetitions; inter-stimulus interval 600 ms). The field was 5–12° in diameter. Short-wave sensitive (S) and medium/long-wave sensitive (ML) cone-isolating pulses and gratings were constructed by convolving marmoset cone spectral sensitivity with the spectral distribution of the monitor phosphors (Tailby et al., 2008b). During measurements of maintained activity, the screen was held at the mean luminance.

The cell class of isolated LGN cells (parvocellular, P; magnocellular, M; or koniocellular, K) was based on a combination of anatomical location (determined via histological electrode track reconstruction) and physiological response profile to visual stimuli. Some recordings from some of the cells presented here were reported in previous papers (Solomon et al., 2014; Townsend et al., 2015; Zeater et al., 2015); all recordings were reanalysed for the present study.

Identification of variable spiking activity

Inter-spike interval (ISI) sequences, defined as the time interval between successive spikes in a spike train, were calculated for each neuron. Given J spikes let t_i be the occurrence time of the ith spike. The ISI sequence is:

$$ISI_i = t_{i+1} - t_i, i = 1, 2 \ldots J - 1. \quad \textbf{(1)}$$

We first introduce a simple measure to examine fluctuations in spiking activity termed spike residuals. A linear regression is applied to the spike index i and spike time t_i. Here, i acts as the dependent variable and t_i the explanatory variable. Linear regression fits a straight line following $\hat{\imath} = a_o t_i + a_1$, where $a_0 = Cov(t_i, i)/Var(t_i)$ and $a_1 = \langle i \rangle - a_0 \langle t_i \rangle$, where, $\langle i \rangle$ and $\langle t_i \rangle$ denotes

7

the expected value of i and t_i, respectively, $Cov(t_i, i)$ denotes the covariance between the two signals, t_i, and i, and $Var(t_i)$ the variance of t_i. Thus, the spike-index residual, e_j,

$$e_j = i_j - \hat{\imath}_j, j = 1, 2 \dots J - 1 \quad (2)$$

is the difference between the value of the spike index predicted by the regression $\hat{\imath}$, and the measured value i. The spike-time residual preserves all inter-spike intervals (i.e. no temporal binning is required) thus giving a simple and parameter-free representation of spiking dynamics.

Identification of fractal spiking activity

Fluctuations of spike counts can also be quantified using the Fano-factor, which is defined as the variance of the spike count divided by the mean spike count across trials (Goris et al., 2014). Here, we used the Fano-factor time curve as introduced by Teich et al. (1997). Given a spike count rate of $N_\tau(t)$ calculated using non-overlapping windows of duration τ, the Fano-factor time curve, F_τ is

$$F_\tau = \frac{Var(N_\tau(t))}{\langle N_\tau(t) \rangle}. \quad (3)$$

If spike times are Poisson-distributed, then $F_\tau = 1$ for any τ as the variance of a Poisson process is equal to its mean for all window sizes. Any deviation from unity thus implies a divergence from Poisson-like activity. If the signal has regularity then the variance decreases as window size increases, and $F_\tau \to 0$. If the signal is fractal then the Fano-factor appears as a straight line on a log-log plot of F_τ against τ and can be fitted as a power-law function with exponent α: $F_\tau \sim \tau^\alpha$ (Teich et al., 1997; Lowen et al., 2001). The slope of the Fano-factor time curve therefore provides an estimate of fractal scaling. We also characterise the Fano-factor time curve by the divergence point, τ_X, the window-width where the curve diverges from unity and follows a power-law function. To obtain the divergence point a power law function, $F_\tau = a\tau^\alpha$, where a is an arbitrary constant, is fit to power-law segment of the Fano-factor time curve using a Levenberg-Marquardt nonlinear least squares algorithm and the fit is used to solve for the divergence point τ_X where $F_\tau = 1$. In calculating the Fano-factor time curve we increased the window width from a minimum of $\tau = 1$ ms to a maximum of $\tau = \tau_{max}/10$, where τ_{max} is the duration of the recording, to avoid limited sample size effects.

8

Characterising the coupling of a neuron to the population activity

To characterize the coupling of each neuron to the population activity, we adopted methods introduced by Okun et al. (2015). The spike-triggered population rate, $stPR_i$, of each neuron i to population activity is given by

$$stPR_i(\iota) = \frac{1}{\|f_i\|} \int_0^{\tau_{max}} f_i(t + \iota) \sum_{j \neq i} \left(f_j(t) - \langle f_j \rangle\right) dt, \quad (4)$$

where t is time, ι is lag, $f_i(t)$ represents the smoothed spike rate of neuron i, τ_{max} is the duration of the recording, $\langle f_i \rangle$ represents its mean spike rate across the whole recording, $\|f_i\|$ is a normalisation value (the number of spikes fired by neuron i) and $1 \leq j < N + 1$, summing over the N recorded neurons and summed j multi-unit activity across all channels.

The size of the population coupling, pc_i, is given by value of the spike-triggered population rate at zero-time lag, $pc_i = stPR_i(\iota = 0)$. The smoothed spike rate, $f_i(t)$, was calculated by binning spikes with 1 ms resolution and convolving the resultant vector with a Gaussian of half-width $12/\sqrt{2}$ ms (Renart et al., 2010). Control analyses were performed on shuffled surrogate datasets, which were generated as described in the Statistics section. To compare across recordings, we normalize the population coupling by the median population coupling of the surrogate shuffled spike data.

Identification of correlated activity

The spike count correlation, r, is the Pearson correlation coefficient between the maintained spike counts of two simultaneously recorded neurons. Given a pair of neurons, X and Y, with maintained spike counts $N_X(t)$ and $N_Y(t)$, the correlation r_{XY} is given by

$$r_{XY} = \frac{Cov(N_X(t) - < N_X(t) >, N_Y(t) - < N_Y(t) >)}{\sqrt{Var(N_X(t) - < N_X(t) >)} \sqrt{Var(N_Y(t) - < N_Y(t) >)}}. \quad (5)$$

For our analysis the maintained spike counts were calculated using non-overlapping 200 ms bin then convolved with a Gaussian kernel (σ = 200 ms) according to Renart et al. (2010). As changing brain states across a long recording epoch could potentially alter r_{XY}, we compared pairwise correlations across the first and second half of the recording. No significant differences in r_{XY} were found.

Characterising functional connections

9

Functional connections between neuron pairs were calculated using r_{XY} within each recording. A functional connection, fc_{XY}, is defined as existing between 2 neurons if the pairwise correlation $r_{XY} > \langle r_{pop} \rangle + \sigma_{r_{pop}}$, where r_{pop} represents all pairwise correlations recorded, $\langle r_{pop} \rangle$ is the mean value, and $\sigma_{r_{pop}}$ is the standard deviation. Using the resultant binarized adjacency matrix, we calculated the degree of connectedness, $q_i = \sum_j fc_{ij}$, defined as the total number of functional connections connected to a given neuron i (van den Heuvel and Sporns, 2011).

Rescaled range analysis

In complementary analysis to the Fano-factor time curves outlined above, we characterized spike rate fluctuations, $f(t)$, as a continuous self-similar process satisfying

$$f(at) = |a|^H f(t), (6)$$

where a is an arbitrary constant, t is time, and *H* is the Hurst exponent (Beran, 1992). We calculated the Hurst exponent using rescaled range (R/σ) analysis as described in Weron (2001). To calculate the rescaled range, a neuron's spike rate measured across a recording duration, τ_{max}, is divided into d non-overlapping subseries of length n. For each subseries, $m = 1, \dots, d$: we find the mean, $\langle f \rangle_m$, and standard deviation, σ_m, and normalise the data, $f_{i,m}$, by subtracting the sample mean $V_{i,m} = f_{i,m} - \langle f \rangle_m$. We then calculate the cumulative time series, $Z_{i,m} = \sum_{j=1}^{i} V_{i,m}$ for $i = 1, \dots, n$, and the range of each subseries $R_m = \max Z_{i,m} - \min Z_{i,m}$, finally, we calculate the mean rescaled range, $\frac{R_m}{\sigma_m}$, for each subseries of length n

$$\left(\frac{R}{\sigma} \right)_n = \frac{1}{d} \sum_{m=1}^{d} \frac{R_m}{\sigma_m}. (7)$$

Asymptotically, the rescaled range follows the relation, $\left(\frac{R}{\sigma} \right)_\tau \propto c\tau^H$, where $\tau = n\Delta t$ is the window width, Δt the window the spikes are binned in to calculate the firing rate, c is an arbitrary constant, and H is the Hurst exponent. In the present study, when calculating the Hurst exponent of the spike rate, $f(t)$, spikes were binned into non-overlapping counting windows of duration $\Delta t = 500$ ms (Thurner et al., 1997) and the subseries lengths n were chosen such that τ ranged from a minimum of $\tau \sim 6$ s to a maximum of $\tau \sim \frac{\tau_{max}}{4}$ s in 50 logarithmic steps; we tested other window widths from $\Delta t = 200$ ms to 3 s and obtained similar results. Furthermore, the reader should note that the Hurst exponent is related to various other fractal measures; for example another typical fractal

10

measure is detrended fluctuation analysis (DFA) where the DFA exponent a, is equal to Hurst H via $a = H + 1$ (Hardstone et al., 2012).

Fractal Brownian motion

Fractal Brownian motion (fBM) is a non-stationary fractal stochastic process (Mandelbrot, 1982), which can also be parameterised by the Hurst exponent H, satisfying Eq. 6. The commonly used definition of $fBM(t)$ is $fBM(t) = \int_{-\infty}^{\infty}[K(t - s) - K(-s)]dB(s)$, where $K = t^{H-\frac{1}{2}}/\Gamma(H + 1/2)$ for $t \geq 0$ and $K = 0$ for $t < 0$, $0 \leq H \leq 1$, Γ is the Gamma function, $B(s)$ is ordinary Brownian Motion, and t, s are time increments (Abry and Sellan, 1996). From this definition the variance of fractal Brownian motion increments is given by $Var\big(fBM(t) - fBM(s)\big) = a|t - s|^{2H}$ where a is a positive constant (Abry and Sellan, 1996). The value of H determines the structure of fBM as follows. When the value of H lies between 0 and 0.5, the fBM is negatively correlated: an increase in spike rate is typically followed by a reduction, and a reduction is typically followed by an increase. When H lies between 0.5 and 1, the fractal process is positively correlated, that is, an increase in spike rate is typically followed by another increase, and a reduction in spike rate is typically followed by further reduction. Thus, long-range correlations exist in the spike rate for $H \neq 0.5$. When $H = 0.5$, successive changes in spike rate are independent ("pure" Brownian motion). The fBM signals are created as a cumulative summation of fractal Gaussian noise generated using bi-orthogonal wavelets as in Abry and Sellan (1996) and Bardet et al. (2003) and generated using the MATLAB function *wfbm.*

Globally modulated fractal stochastic process

To determine the relation between fractal Fano-factor time curves and neural population coupling we developed a fractal stochastic model, which combines fractal fluctuations of spike rate with a global modulatory gain term (Churchland et al., 2011; Ecker et al., 2014; Goris et al., 2014). The model is an extension of the commonly used model in which the spike count N follows an inhomogeneous Poisson distribution:

$$p(N|f(t), \Delta t) = \frac{f(t)\Delta t}{N!}e^{-f(t)\Delta t}, (8)$$

11

here $f(t)$ is the spike rate and Δt, is the counting window. We assume the spike rate arises from the product of two positive-valued signals:

$$f(t) = fBM(t)G(t), (9)$$

where $fBM(t)$ is a fractal process undergoing fractal Brownian motion constrained by the observed Hurst exponents (as described above), and $G(t)$ represents a dynamic global modulatory gain that is identical between simulated neurons. To ensure $f(t)$ is positive the two signals are set to be positive-definite by taking the modulus of the generated signals, $fBM(t) = |fBM(t)|$ and $G(t) = |G(t)|$. As a minimal assumption, we set the global rate to be Gaussian (white) noise ($\langle G \rangle = 4$ Hz, $G_\sigma = 2$ Hz) where the signal is generated in 1 ms increments. Global modulatory gain can represent effects such as changes in neuromodulation from arousal levels, attention, or anaesthesia (Goris et al., 2014; Shine et al., 2019). Furthermore, the simulated individual neuronal fractal rate $fBM(t)$ is scaled such that the simulated cells mean firing rate, $\langle fBM(t) \, G(t) \rangle$ matches the empirically observed cell population mean spike rate $\langle f \rangle_X$, where X = P, M, K, or MT, i.e., $\langle fBM(t) \, G(t) \rangle = \langle f \rangle_X$. This is achieved by scaling the generated $fBM(t)$ to ensure the condition that $\langle fBM(t) \rangle = \langle f \rangle_X / \langle G(t) \rangle$ is met, this scaling maintains the fractal relationship as a scaled fractal is itself fractal. Finally, we require that $fBM(t)$ cannot be strongly anti-correlated with $G(t)$, $r_{G(t) \, fBM(t)} > -0.3$, as $G(t)$ is generated first we achieve this condition by discarding generated $fBM(t)$ that fail the criterion; this assumption ensures the simulated neuronal spike rates predominantly range between slightly anti-correlated to strongly correlated, consistent with experimental findings (Okun et al., 2015).

Statistics

Statistical analyses and graphing were conducted using MATLAB (R2016b, MathWorks Inc., Natick, MA, USA). All values are reported as the mean μ and standard deviation σ. Correlations were assessed using Pearson's correlation coefficients and Spearman rank coefficient (as specified). Statistical comparisons for measured values containing multiple groups were compared using the Wilcoxon non-parametric rank sum test. Two surrogate data series were generated. In the first, we randomly shuffled ISI times across the entire recording duration for a recorded neuron and generated surrogate neuronal spike times as their cumulative summation. This surrogate dataset removes inter-spike dependencies and long-term spike correlations while preserving the ISI

distribution. This surrogate dataset tests the null-hypothesis that surrogate neurons with identical inter-event distribution to the recorded neurons can reproduce the observed spike dynamics. The second surrogate data set was generated by randomly swapping spike pairs between all simultaneously recorded neurons (as in Okun et al., 2015) destroying inter-neuronal correlations. To ensure a sufficient number of swaps are performed to randomize the surrogate data, we swap all recorded spikes at least once. By swapping spike pairs, we ensure each surrogate neuron retains the same number of spikes across the entire recording as the recorded neurons and the shuffling preserves the population spike rate. This surrogate exercises the null-hypothesis that population coupling varies according to differences in mean spike rate or the temporal properties of the population spiking activity. Model comparisons were made using the Bayesian information criterion (BIC; Schwartz, 1978) after fitting data using a Levenberg-Marquardt nonlinear least squares algorithm. Statistical comparisons between distributions were compared using a two-sample Kolmogorov-Smirnov test.

Results

The activity of 49 single LGN cells was measured at 10 recording sites in three marmosets. The functional class of each LGN cell was determined by a combination of histological reconstruction of the recording sites (Fig. 1A) and visually-evoked responses to cone-isolating and achromatic contrast pulses. Example responses of three simultaneously recorded neurons to ML cone and S cone isolating contrast increments and decrements are shown in Fig 1B-D. Of the 49 isolated cells, 12 were classified as parvocellular (P-cells), 5 as magnocellular (M-cells) and 32 as koniocellular (K-cells); the 49 isolated cells came from 10 recordings comprising 12, 12, 5, 4, 3, 3, 3, 3, 2, and 2 well isolated cells. Similar measurements were made from 30 cells in area MT (15 randomly selected cells from each of two separate marmosets; Townsend et al., 2015). Our analyses of spiking dynamics are based on measurements of the maintained activity (i.e. in absence of patterned visual stimuli) of these cells.

Fractal variability of maintained activity

Spike rate in both LGN and MT shows super-Poisson dynamics (a larger variance than a Poisson process with the same mean). Figure 2A demonstrates the variance to mean relationship of all cells, for spike counts binned in windows of $\tau = 10$ s. The strength of fluctuations as measured by the

13

coefficient of variation increases from P-cells to K-cells (p = 0.005, Wilcoxon non-parametric rank sum test), from M-cells to K-cells (p = 0.05), and from LGN to MT (p < 0.001). The super-Poisson variability in LGN and area MT cells is robust for all $\tau >$1s and is due to nonstationary fluctuations of the spike rate.

We used the spike-index analysis to visualise variability at multiple temporal scales. The spike-index residual (see Methods) preserves all inter-spike intervals (i.e. no temporal binning is required) and offers a simple parameter-free representation of spiking dynamics. Spike-index and spike residual are demonstrated for three LGN cells in Figure 2B and C respectively. Figure 2D compares the spike-index residual for one K cell at several timescales. In each case, the residual appears as a slow-up, rapid-down sawtooth pattern over time. The appearance of similar patterns of variability across multiple scales is a signature of a fractal process.

We next used Fano-factor time curve and power spectrum analyses to quantify the fractal structure of the spike variability. The Fano-factor as typically calculated is a biased metric, biased by the window, τ, used to bin the spike count (Nawrot, 2010), thus, we overcome this bias by calculating the Fano-factor time curve (differing τ). As expected (Croner et al., 1993; Victor et al., 2007), at short window sizes ($F_{1\ ms}$) the Fano factor is close to unity: for short windows the spike count is an approximation of the Bernoulli process and in each small interval we observe either 1 spike with probability p or 0 spikes with probability $1 - p$. However, beyond a critical window size, τ, which we call the *divergence point*, the Fano-factor increases, with respect to the empirical limit $F_\infty = \lim_{\tau \to \infty} FF_\tau$, as observed in our data the limit appears unbound and increases as a power-law curve. This finding is evidence for fractal dynamics. If, for example, the spike rate was oscillatory the FF would increase above unity before decreasing below unity at τ = the period of the oscillation. We validate this assertion below in Fig. 7.

We observed a large variability in F_τ (Fig 3A-D) both within (individual neurons are shown by faint grey lines) and between different populations (averages are shown by coloured lines). The slope of the power-law segment of the population mean F_τ is similar and close to 0.7 in all LGN subclasses, but the slope is shallower in MT, $\sim$ 0.5. By contrast, the arrows in Fig 3E show that the divergence point occurs at shorter time windows for K (τ_K: μ = 0.18 s, σ = 0.04 s), than for P (τ_P: μ = 1.5 s, σ = 0.1 s), or M (τ_M: μ = 1 s, σ = 0.1 s) cells (p < 0.01, Kruskal-Wallis test). Interestingly, we find that the divergence point for K-cells is closer to that for cortical area MT (τ_{MT}: μ = 0.01 s, σ = 0.01 s).

14

Fano-factor time curves for MT recordings terminate earlier than those for LGN because the recording epochs in MT were briefer (~300 s in MT compared to ~1200 s in LGN).

We next computed the average power-spectrum for each cell population, and asked whether the Fano-factor time curves are consistent with the power spectrum, as is expected by theory (Melsa and Sage, 1973). Power spectra were calculated for spikes binned in non-overlapping windows of 1 ms. Because the spikes are binned in windows smaller than the mean interspike interval, the resultant power-spectrum, $P(f)$, is an estimate of the point process (Melsa and Sage, 1973). We averaged across recordings and found the mean power-spectrum of each cell class exhibits power-law $1/f$ decay characterised by a straight line in log-log axis (Fig. 3F, dotted lines). These results are congruent with the expected relationship between Fano-factor scaling exponent, $F_T \sim T^\alpha$, and power-spectrum exponent, $P(f) \sim 1/f^\alpha$, for all cell classes (Teich et al., 1997). For example, the power-spectrum exponent for area MT (P_{MT}) is close to 0.5 ($P_{MT}(f) \sim 1/f^{0.5}$) as is the Fano-factor scaling exponent ($F_{T\,MT} \sim T^{0.5}$). Congruent values were also found for P-cells and M-cells: $P_{P,M}(f) \sim 1/f^1$; $F_{T\,P,M} \sim T^{0.7}$ and K-cells: $P_K(f) \sim 1/f^{0.8}$; $F_T \sim T^{0.7}$. To ensure the suitability of the power-law fit of the Fano-factor time curves and power-spectra, the Bayesian information criterion (BIC; Schwartz, 1978) was calculated for a power-law curve, an exponential curve, and a logarithmic curve. Curve parameters were estimated using a Levenberg-Marquardt nonlinear least squares algorithm. The results are summarized in Table 1, which shows that the Fano-factor time curves were best fit by a power-law curve across multiple orders of magnitude for all cell types studied. In sum, the pooled Fano-factor time curves and spectral analyses indicate consistently that the LGN and cortical spike trains show fractal property.

The reader should note at this stage that we see additional signs of non-fractal complex dynamics in the measured spike trains. For example, some cells show non-monotonic rise in the Fano-factor time curve beyond the divergence point (faint grey lines, Fig. 3A–D), and the spectra in Figure 3F include peaks which rise above the lines of fractal slope. We did not attempt to model these additional complexities. They do not affect our main conclusion that fractal dynamics give a better explanation for the observed spike trains than do exponential or logarithmic dynamics.

We tested our Fano-factor and frequency analyses on surrogate datasets by randomly shuffling the ISIs of each neuron. The surrogate point process formed from the shuffled intervals has the same distribution of ISIs but the correlations between spikes are destroyed. In other words, the surrogate datasets are equivalent to a sample from a renewal process with ISI distribution

15

equivalent to the original point process (Melsa and Sage, 1973). As expected we find that shuffling the ISI times of each neuron flattens the Fano-factor time curve to unity (Fig. 3E), and flattens the power spectrum to the mean spike rate (Fig. 3F). Thus, when compared with the surrogate data for all LGN and MT neurons at large temporal windows spiking activity is significantly different from surrogate uncorrelated spiking data with an identical ISI distribution (at τ = 2 s: MT-cells, μ = 16, σ = 8; K-cells, μ = 4.7, σ = 4.0; P-cells, μ = 1.6, σ = 0.4; M-cells μ = 1.8, σ = 0.5; Fig. 3E). In all cases these values are larger than values for the surrogate data (μ = 1.1 σ = 0.1, p < 0.001, Kruskal-Wallis test).

Because the above analyses indicate fractal variability, we also performed rescaled-range analysis, which provides a measure of fractal fluctuations from a different perspective (Eq. 6, Eq. 7). The rescaled-range is the ratio between the range of the cumulative normalised spike rate and its standard deviation at each temporal scale. The slope of the resulting power-law increase of rescaled range is the Hurst exponent (see Methods). The Hurst exponent H is a dimensionless quantity that characterizes the long-range temporal correlations: for $0 \leq H < 0.5$ correlations are negative; for $0.5 < H \leq 1$ correlations are positive. As H increases the variability of fractal stochastic process increases. At this point we note that fractal Brownian motion (fBM) can also be characterised by the Hurst exponent: in a later section we use fBM to develop a model which explains the experimentally observed data.

As shown in Figure 4, the rescaled range analysis reveals fractal fluctuations that are well described by a power-law function, $\left(\frac{R}{\sigma}\right)_\tau \sim \tau^H$, (Fig. 4 left column; dashed line) as the curve extends across multiple orders of magnitude across all cells. The slope of the power-law fit is the Hurst exponent. As the Hurst exponent is calculated on the spike-rate calculated using a counting window $\Delta t = 500$ ms it has a limited range and only asymptotically scales as the Hurst exponent (Weron, 2001), thus, to ensure the suitability of the power-law fit of the rescaled range analysis the Bayesian information criterion (BIC) was again calculated as above (Table 1) yielding a result congruent with the Fano-factor time curve analysis, that is, the power-law model best fits the data indicating fractal spike rates. The spike rate of an example cell from each population is shown in the centre column of Figure. 4. Importantly, we find that the Hurst exponent is similar within each cell class, and across recordings (Fig. 4, right column), and is always less than 0.5 (indicating negative long-timescale correlations). Furthermore, the Hurst exponent increases from LGN to area MT and is lower in P-cells and M-cells cells than in K-cells. The population mean, μ, and standard deviation, σ, of the Hurst exponent distribution are P-cells, $\mu = 0.1, \sigma = 0.01$; M-cells, $\mu = 0.1, \sigma = 0.01$; K-cells, $\mu =$

16

0.18, $\sigma = 0.02$; and MT-cells, $\mu = 0.24, \sigma = 0.03$. The K-cells show marginally larger Hurst exponents than P-cells ($p = 0.007$, Wilcoxon non-parametric rank sum test) and M-cells ($p = 0.02$). Similarly, MT-cells show larger Hurst exponents than P-cells ($p = 0.001$), M-cells ($p < 0.001$, Kruskal-Wallis test), and K-cells ($p < 0.001$, Kruskal-Wallis test). These results are consistent with our earlier finding that the mean-normalized variance (Fano-factor) in K-cells is greater than that in P-cells or M-cells, and that the mean-normalized variance of MT-cells is greater than that of LGN cells.

Population coupling and variable spiking are related

Studies of visual cortical area V1 in mouse and macaque monkey have shown the activity of individual neurons can range from weakly to strongly coupled (correlated) to the population activity (Okun et al., 2015). In this section we show that that diverse coupling is a feature of spiking activity in the LGN (most prominently in K-cells) and is also a property of MT-cells. Figure 5A shows examples of K-cell, M-cell, and P-cell spike-triggered population rate ($stPR$). To normalise and compare across recordings we use the median value of population coupling ($pc = stPR$ at zero-lag) after shuffling (see Methods: *Characterising the coupling of a neuron to the population activity*). As shown in Fig. 5B, population coupling in LGN neurons varies from strongly correlated to anti-correlated with the population activity. The pc coefficients range from -0.5 to 4, displaying anti-correlated to strongly correlated population coupling. A similar pattern was observed within MT, with values ranging from -1 to 4 (Fig. 5D, E), which is also consistent with that described in V1 of mouse and macaque (Okun et al., 2015). As expected, shuffling spike times destroys the broad population coupling yielding μ = 0.99 and σ = 0.1 (Fig. 5B, E). The shuffling removes non-stationarities of individual neurones but preserves mean spike rates as well as temporal fluctuations in the population spike rate. This result therefore confirms that diverse coupling of neurons is not a statistical artefact due to the average spike rate of individual neurons. The K-cells (μ = 1.2, σ = 0.9) and MT-cells (μ = 0.9, σ = 0.6) demonstrate a broader distribution of population coupling than M-cells and P-cells (μ = 0.9, σ = 0.4).

Our analyses show that spiking variability and population coupling is stronger in K-cells than in M-cells or P-cells. We therefore asked whether spiking variability is related to population coupling. Indeed, Fig 5C and F show that population coupling, pc, is positively correlated with the Fano-factor ($\tau = 10$ s), for K-cells (r = 0.48, p = 0.01, Spearman rank) and MT-cells (r = 0.6, p < 0.001). The correlation was not significant for M-cells ($r = 0.20$, p = 0.78) or P-cells ($r = 0.27$, p = 0.39), but the sample size for these populations is too small to draw firm conclusions. The result was robust for

17

Fano-factor window sizes $0.5 \leq \tau \leq 100$ s (not shown). In sum, the data appear to reveal an intrinsic relationship between population coupling and spike variability that is common to subcortical and cortical visual centres.

Sub-cortical correlated activity and population coupling

We next apply pairwise correlations analysis to the recorded LGN populations, and show that pairwise correlations are also related to both population coupling and spike variability. Correlated activity is a hallmark of cells that share input or are reciprocally connected. Cortical cells generally exhibit small pairwise correlations that are distance dependent (Smith and Kohn, 2008; Solomon et al., 2014). We measured the pairwise correlations in maintained activity among LGN cell pairs; for example two K-cells would constitute a KK pair while a K-cell and P-cell would constitute a KP pair. The recordings contain 10 PP, 2 MM, 99 KK, 40 PK and 11 MK pairs. No PM pairs were recorded. As shown in Fig. 6A we find PP (μ =0.03, σ =0.05, n = 10), PK (μ =0.06, σ =0.07, n = 40), MM (μ = 0.09, σ = 0.07, n=2) and MK (μ =0.05, σ = 0.08, n=11) pairs are tightly distributed around r = 0, with the median r = 0.05. As expected (Cheong et al., 2011) the KK pairs (μ = 0.08 σ = 0.16, n = 99) show a broader and more positively skewed distribution than the other type-pairings. Correlations between most LGN pairs are small, and decrease slightly with distance (Fig. 6B). Interestingly, some KK pairs show high correlations at distances as far as 600 μm, suggesting that these correlations do not originate from visuotopically organised inputs but perhaps from broadly organised inputs from other sub-cortical areas.

Population coupling in mouse V1 was suggested to reflect greater synaptic connectivity (Okun et al., 2015). To address this possibility in LGN, we calculated functional connectivity maps (Buckner et al., 2011), where the existence of a functional connection is determined by the strength of pairwise correlation coefficients. An example of a functional connectivity map between simultaneously recorded pairwise neurons is shown in Fig. 6C. We first looked at the spatial spread of functional connections by ignoring all small or negative functional connections, $r < 0.1$, and calculating the degree of connectedness, q, for each neuron (Poli et al., 2015). For the purposes of these analyses, connections were taken to be undirected and unweighted. The degree of connectedness q (See Methods) quantifies the number of functional connections of a neuron with its neighbours. We find that P-cells (μ = 1.1, σ = 2.1) and M-cells (μ = 1.2, σ = 1.9), have lower q than K-cells (μ = 2.6, σ = 3.3; Chi-square variance test, p < 0.001 for both comparisons). Figure 6D shows connections of 4 example neurons from the functional connectivity map in Fig. 6C; here it is evident

18

that functional connections can extend across layers of the LGN and between functionally distinct cell types.

We next asked if there is correlation between the number of functional connections a neuron receives and its population coupling. We limited our comparison to recordings containing more than 10 isolated K-cells. Figure 6E compares the normalised population coupling (pc) and the total number of functional connections (q). Population coupling increases with the number of functional connection (Spearman rank correlation coefficient = 0.66, p < 0.005). This result expands our understanding of population coupling to include inferred connections to K-cells within the LGN. It should be noted that the calculation of functional connections (strongly correlated neurons) is extremely similar to population coupling in terms of the data analysis calculations and it is no surprise that they are strongly correlated.

As the final step of our empirical analysis, we asked how the variable spiking of each neuron relates to the degree of connectedness. Figure 6F shows that Fano-factor ($\tau = 10$ s) and the total number of functional connections are marginally correlated (Spearman rank correlation coefficient = 0.48, p = 0.05). Thus, K-cells with stronger functional connections are not only more variable but are also more coupled to the population activity, revealing a relationship between pairwise correlations and spike rate variability.

Unifying explanatory model

In this section, we show that a fractal stochastic process with a global modulatory gain can provide a unifying model for our empirical data. Although previous studies have used inhomogeneous Poisson processes to reproduce variability in maintained activity (Teich et al., 1997) and evoked variability (Ecker et al., 2014; Goris et al., 2014), they were unable to explain both diverse population coupling and fractal spiking. Here we model the rate of an inhomogeneous fractal Poisson process, $f(t) = fBM(t)$G(t), as the product of an intrinsic process of fractal Brownian motion, $fBM(t)$ and a global modulatory gain, $G(t)$, which is assumed to be white noise ($\langle G \rangle = 4, G_\sigma = 2$) (see Methods). When simulating a cell from a given population, we randomly sample the Hurst exponent from a normal distribution whose parameters are matched to our empirical data (Fig. 4): P-cells, $\mu = 0.1, \sigma = 0.02$; M-cells, $\mu = 0.1, \sigma = 0.02$; K-cells, $\mu = 0.18, \sigma = 0.02$; MT-cells, $\mu = 0.25, \sigma = 0.02$ and we normalise individual $f(t)$ such that the population spike rate distribution matches the empirical data. Thus, the generative model is empirically constrained to produce activity that matches both the Hurst and average spike rate distribution seen in experimental data.

19

Figure 7 compares our fractal inhomogeneous Poisson model to other plausible types of non-stationary spike dynamics. We first showed that 20 simulated neurons with a dynamic rate undergoing fractal Brownian motion (Fig. 7A) reproduce the fractal signature in the Fano-factor time curve. We then simulated three other inhomogeneous Poisson models by modifying $fBM(t)$, while preserving the global gain modulation $G(t)$ and the mean spike rate. Firstly we removed the fractal component of the model (by setting the Hurst exponent to 0.5). This change destroyed the increase in Fano-factor for increasing window (Fig. 7B). Secondly we set the dynamic rate to oscillate at a rate of 1/30 Hz. In this case, the Fano-factor peaks at $\tau \sim 10$ s before decreasing below unity at $\tau \sim 30$ s, which corresponds to the period of the oscillation (Fig. 7C). Finally, we randomly drew spike rates from a heavy-tailed lognormal distribution ($\mu = 2$, $\sigma = 2$) and found the Fano-factor does not increase above unity (Fig. 7D). Thus, our model (through the inclusion of a fractal rate) provides a simple and minimal method to reproduce the empirically observed power-law increase in the Fano-factor time curve.

Comparison to experimental data.

The model quantitatively reproduces the temporal spike patterns observed experimentally. Figure 8A (left column) shows the simulated spike rate of a P-cell (upper row), a K-cell (centre row) and an MT-cell (lower row). In these examples the global modulatory gain is identical, and the Hurst exponent used to generate the fractal Brownian motion is varied depending on cell type. We found a good match between simulated and recorded spike rates for each cell class (Fig. 8A, right column). After simulating the same number of neurons for each cell-type as experimentally recorded we found the model produced cell-type population ISI distributions (pooled ISIs across all cells of a given type; Fig. 8B left column) that match the empirical data for P (p = 0.03), M (p = 0.01), K (p < 0.001), and MT cells (p = 0.01; two-sample Kolmogorov-Smirnov test; Fig. 8B right column). Removing the fractal component of the model (by setting the Hurst exponent to 0.5, as in Fig. 7B) destroyed the quantitative correspondence for all cell groups (p > 0.2 for all comparisons; two-sample Kolmogorov-Smirnov test). Consistent with the experimental recordings (Fig. 2A) we found (Fig. 8C) simulated cells reproduce the same spike-count variance to spike-count mean ratio qualitatively and the K-cells display more spike-count variability than P-cells and M-cells do (Cheong et al., 2011). Thus, an increasing Hurst exponent captures the variable spiking dynamics in the observed data.

The simulated spike trains resemble the experimentally observed spike trains, but of course we need to show deeper connections between our model and the population data. We therefore

20

asked whether our fractal stochastic model can explain the observed differences in Fano-factor time curves between the different (K-cell, P/M-cell, MT-cell) groups as seen in Figure 3E. Figure 8D demonstrates the simulated Fano-factor time curves (pale lines show individual simulations; the dark line shows population mean ±SEM). In close agreement with the experimentally observed Fano-factor time curves (Fig. 3E), the simulated curves are unity for small windows before increasing as a power-law function as expected for a fractal process generated using fBM (Teich et al., 1997). Further, we find the divergence points (arrows) are quantitatively comparable to the experimentally observed divergence points (τ_{MT} $0.01s < \tau_K$ $0.1s < \tau_{P/M}$ $1s$) for each of the cell populations and inversely proportional to the Hurst exponent of each cell-type population. Thus, fractal Brownian changes in spike rate and cell-type specific Hurst exponents are required for our model to reproduce the empirical data.

We next asked whether our inhomogeneous fractal model could also reproduce diverse population coupling by allowing the global modulatory signal G_σ to vary (see Methods). We found diverse population coupling that matches the recorded data under only a restricted range of global modulation G_σ variability. Figure 9A shows five example $stPR$ traces (Fig. 9A left column) and the population coupling distribution (Fig. 9A right column) of 40 simulated K-cells without global modulation ($G_\sigma = 0$ Hz), here the normalized population coupling (red) is extremely broadly distributed before ($\mu = 0.1$ and $\sigma = 6$; Fig. 9A right column red) and tightly distributed after spike-pair shuffling ($\mu = 1.04$ and $\sigma = 0.15$; Fig. 9A right column blue). The broad distribution of normalized population coupling is expected as the simulated cells are uncorrelated. On the other hand, under strong global modulation variability ($G_\sigma = 10$ Hz), the $stPR$ traces overlap (Fig. 9B left column) and the normalized population coupling are tightly distributed both before ($\mu = 1.07$ and $= 0.15$; Fig. 9B right column red) and after ($\mu = 1.07$ and $\sigma = 0.15$; Fig. 9B right column blue) spike-pair shuffling. Here, the tight distribution around $pc = 1$ shows that spike rates of all the simulated neurons are strongly correlated. Finally, as shown in Figure 9C, under a restricted ("Goldilocks") range of global modulation variability between these two extremes, (G_σ = 1 Hz to 4 Hz), we found the simulated population coupling is intermediately distributed and closely resembles the experimentally observed distribution of K-cells ($\mu = 1.2, \sigma = 0.9$, cf. Fig. 5B). For example, at $G_\sigma = 2$ Hz, the simulated $stPR$ traces (Fig. 9C left column) and the normalized population coupling are broadly distributed ($\mu = 0.78, \sigma = 1.18$; Fig. 9C right column red) and become narrowly distributed ($\mu = 1.01, \sigma = 0.15$; Fig. 9C right column blue) after spike time shuffling. The difference between normalized population coupling and spike-pair shuffled population coupling implies the

21

population coupling reproduced by the model is not due to differences in mean spike rates or temporal properties of the population rate. Congruent results were obtained from simulated sets of P-cells, M-cells, and MT-cells (data not shown).

Our recorded data in LGN and MT showed an intrinsic relationship between diverse population coupling and fractal Fano-factor time curves (Fig. 5C, 5F). Under the conditions shown in Figure 8C and simulating 400 K-cells, the inhomogeneous fractal model reproduces this relationship ($r = 0.42, p < 10^{-17}$, Fig. 10A). We note here that the relationship between Fano-factor and normalised population coupling, pc, is consistent with experimental findings (Okun et al., 2015). Within our model each simulated neuron receives the same global modulation, thus, the difference in Fano-factor and population coupling arise from the individual neuronal fractal rates $fBM(t)$ generated with differing Hurst exponents. We observe the pc is positively correlated with the Hurst exponent ($r = 0.29, p < 10^{-7}$, solid line Fig.10B). Less variable simulated cells (smaller than average Hurst exponent) are centered around the shuffle normalized median population coupling $pc \sim 1$ extending into negative pc, whereas, the more variable simulated cells (larger than average Hurst exponent) the population coupling increases with Hurst exponent. This result is expected as the magnitude of the population coupling is proportional to the variance of the spike rate for cells with identical mean spike rates (Eq. 4). Finally, we found that as the Hurst exponent increases the variance of the spike rate increases ($r = 0.46, p < 10^{-21}$; Fig. 10C). This can be understood by the variance of fractal Brownian motion increments given by $Var\big(fBM(t) - fBM(s)\big) = a|t - s|^{2H}$ where a is a positive constant and t, s are time increments (Abry and Sellan, 1996), i.e. given two $fBM(t)$ signals with identical mean spike rate the signal with a larger Hurst exponent will possess greater variance ('burstier') and as a result a larger Fano-factor. In other words, a neuron's intrinsic fractal variability (Hurst exponent) can explain the correlation between apparently independent properties of spike variability and diverse population coupling.

Discussion

Our results indicate that fractal spike dynamics and diverse coupling to population activity are general properties extending across sub-cortical (LGN) and cortical (MT) visual areas. The fractal dynamic and population coupling properties are linked, in that neurons showing greater fractal fluctuations are more correlated to the local population activity. An inhomogeneous fractal Poisson process with global modulatory gain can explain this linkage, as well as account for the transition from Poisson-like dynamics at short timescales to fractal dynamics at longer timescales. Our results

22

thus establish a unified account of two dynamic properties of neural spike activity: fractal spike patterns (Teich et al., 1997) and diverse population coupling (Okun et al., 2015), which to date have been treated independently and which previous rate-based stochastic modelling studies (Ecker et al., 2014; Goris et al., 2014) could not reproduce. The computational simplicity of our model means empirical spiking dynamics can be readily simulated and used to guide more biophysiological models to drive further insights into neural dynamics.

Despite our successful application of a fractal-based model to the observed spike trains it could be argued that (as with any model) the fractal analysis does not offer a complete characterisation of the data. Most importantly, as noted in connection with Figure 3, we see additional signs of non-fractal complex dynamics in the observed spike trains. We did not further elaborate our model to capture such complex dynamics, but our main conclusions regarding differences between the cell classes (for example, the tighter coupling of K-cell activity to population activity) are relative, and therefore not an artificial by-product of the fractal analysis. In contrast, our fractal-based model contains the minimal additions required to reproduce empirically observed fractal variability and diverse population coupling.

Recordings were conducted under sufentanil anaesthesia, which constitutes a limitation to our study. Most pertinently, during recordings the EEG spectrum was dominated by sub-alpha frequencies, that is, quite different to waking state. Alitto et al. (2011) showed LGN cell responses to visual stimuli remain consistent between alert and anaesthetised states (although maintained rates are reduced under anaesthesia), but it is of course implausible that our results would translate directly to waking animals. Nevertheless, we expect that the broad pattern of results – specifically, the fractal properties of spike trains (Baddeley et al., 1997) and the differences between LGN cell classes (present results), would largely be preserved in alert animals. Analysis of spike trains in waking animals would of course be required to substantiate or refute this prediction.

Fractal nature of fluctuations

Our results extend classical studies of fractal activity in the central nervous system (Teich, 1989; Baddeley et al., 1997; Teich et al., 1997) in two main ways. Firstly, we found fractal spiking activity within both the LGN and cortex, suggesting fractal dynamics could be a general property of ongoing activity in the visual system (and, perhaps, the brain in general). Secondly, we found the spiking variability and population fractal properties vary between parallel visual pathways in the LGN. Furthermore, as we have found that it is neurons with 'burstier' fractal dynamics (larger Hurst value)

23

which are correlated with population spiking activity, larger-scale EEG/MEG recordings which record population activity may be over-represented by the burstier fractal activity (Hardstone et al., 2012).

The fractal feature of neural spike activity indicates that spike rate fluctuations occur over a broad range of time scales and possess long-range correlation. These properties may enable neurons to maximize their information-carrying capacity (Baddeley et al., 1997) and to be capable of rapid reorganization during processing demands (Linkenkaer-Hansen et al., 2001). Furthermore, it could be speculated that intrinsic fractal fluctuations seen at the individual neuronal level are related to behavioural measurements such as fractal fluctuation in reaction time latency (Gilden et al., 1995). Fractal fluctuations of maintained neural activity might underlie such behavioural observations, and may provide an efficient mechanism for exploiting the spatiotemporal structures of scale-invariant natural environments (Ruderman and Bialek, 1994; Munn and Gong, 2018); this may lead to similar fractal spiking dynamics as found in V1 and IT neurons in response to natural movies (Baddeley et al., 1997). Similar to Baddeley et al. (1997) we found that neurons fire sparsely, consistent with using an optimized rate code where the spike rate is constrained to maximize information transmission (Baddeley et al., 1997; Olshausen and Field, 1997).

Relevance to parallel processing in the visual system

We found the divergence point from Poisson-like to fractal Fano-factor time curves decreases from P-cells and M-cells (~1s) to K-cells (~100 ms), and MT-cells (~10 ms). It is possible that the divergence point reflects the timescale over which neuronal populations are recruited for computational tasks. It is interesting to note that MT cells diverge much earlier than thalamic neurons (an order of magnitude compared with K-cells and 2 orders earlier than P/M cells) despite possessing approximately an order of magnitude lower mean spike rate. Furthermore, the fractal slopes of the Fano-factor time curves and power spectrum are consistent within the LGN (~0.7) but shallower within MT (~0.5), and the fractal fluctuations in spike rate characterized by the Hurst exponent increase from P-cells and M-cells (~0.1), to K-cells (~0.18) and MT-cells (~0.25).

The more cortical-like dynamics of K-cells as compared to P-cells and M-cells may be related to other cortical-like properties of K-cells including orientation-selectivity (Cheong et al., 2013), complex (non-phase-locked) responses to periodic grating stimuli (Eiber et al., 2018), and more extensive connections with subcortical centres (Zeater et al., 2019). The K-cells are also distinct from P-cells and M-cells based on their neurochemical signature and cortical projection targets. Whereas P-cells and M-cells are immunoreactive for parvalbumin and project to layer IV of primary visual

24

cortex, K-cells are immunoreactive for calbindin and project to layer IV as well as the superficial layers of primary visual cortex (Hendry and Yoshioka, 1994; Casagrande et al., 2007). This difference feeds into the broader theory of thalamic organization which argues for two parallel thalamocortical systems: a "core" system of parvalbumin reactive cells involved in the relay of sensory signals to cortex and a "matrix" system of calbindin reactive cells involved in synchronization of thalamo-cortical networks (Jones, 2001).

The differences in spike rate fluctuations between LGN and MT lead us to predict that the Hurst exponent increases systematically along the hierarchy of the visual system. In the present study, we recorded from area MT, which receives sparse direct inputs from K-cells (Sincich et al., 2004; Warner et al., 2010) as well as inputs from V1 (Movshon and Newsome, 1996). It is possible that interactions between these inputs contribute to the overall higher Hurst exponent in MT compared to K-cells. Murray et al. (2014) showed an increase in decay time of population autocorrelations along the hierarchy of primate cortical areas. These authors modelled decay time with an exponential distribution. Our results (Fig. 3F). suggests that autocorrelation of spiking activity could alternatively be modelled with a power-law with exponent which increases along the hierarchy of the cortex.

Intrinsic relationships between diverse population coupling and neural variability

The diverse range of population coupling ranging from highly correlated 'choristers', weakly correlated 'soloists', and anti-correlated neurons previously found in V1 of mice and macaque is a simple way to characterise the relationship of a neuron to the population fluctuations (Okun et al., 2015). Here we have extended this observation to both subcortical (LGN) and higher cortical areas (MT), indicating that it may be a general property of visual areas. Furthermore, we have found that diverse population coupling is linked to variable spike dynamics because Fano-factor and the magnitude of population coupling are correlated on a cell-by-cell basis (Fig. 5, Fig. 9). We further confirmed that population coupling is related to pairwise correlations as strongly coupled neurons possess more functional connections (Fig. 6). In sum these empirical results provide a link between spiking properties of individual neurones and connectivity to the neural networks in which they are embedded.

References

Abry P & Sellan F(1996). The wavelet-based synthesis for the fractional Brownian motion proposed
by F. Sellan and Y. Meyer: Remarks and fast implementation. *Appl. and Comp. Harmonic Anal.*,
3, 377–383.

Alitto HJ, Moore BD, Rathbun DL & Usrey WM (2011). A comparison of visual responses in the lateral
geniculate nucleus of alert and anaesthetized macaque monkeys. *J Physiol* **589**, 87-99.

Arieli A, Sterkin A, Grinvald A & Aertsen A (1996). Dynamics of ongoing activity: explanation of the
large variability in evoked cortical responses. *Science* **273**, 1868-1871.

Baddeley R, Abbott LF, Booth MC, Sengpiel F, Freeman T, Wakeman EA & Rolls ET (1997). Responses
of neurons in primary and inferior temporal visual cortices to natural scenes. *Proc R Soc Lond
Ser B Biol Sci* **264**, 1775-1783.

Bardet JM, Lang G, Oppenheim G, Philippe A, & Taqqu MS (2003). Generators of long-range
dependent processes: a survey. *Theory and applications of long-range dependence,* Birkhäuser, 579-
623.

Beran J (1992). Statistical Methods for Data with Long-Range Dependence. *Statistical Science* **7**, 404-
416.

Buckner RL, Krienen FM, Castellanos A, Diaz JC & Yeo BT (2011). The organization of the human
cerebellum estimated by intrinsic functional connectivity. *J Neurophysiol* **106**, 2322-2345.

Casagrande V, Yazar F, Jones K & Ding Y (2007). The morphology of the koniocellular axon pathway
in the macaque monkey. *Cereb Cortex* **17**, 2334-2345.

Cheong SK, Tailby C, Martin PR, Levitt JB & Solomon SG (2011). Slow intrinsic rhythm in the
koniocellular visual pathway. *Proc Natl Acad Sci USA* **108**, 14659-14663.

Cheong SK, Tailby C, Solomon SG & Martin PR (2013). Cortical-like receptive fields in the lateral
geniculate nucleus of marmoset monkeys. *J Neurosci* **33**, 6864-6876.

Churchland AK, Kiani R, Chaudhuri R, Wang XJ, Pouget A & Shadlen MN (2011). Variance as a
signature of neural computations during decision making. *Neuron* **69**, 818-831.

26

Croner LJ, Purpura K & Kaplan E (1993). Response variability in retinal ganglion cells of primates. *Proc Natl Acad Sci USA* **90**, 8128-8130.

Dayan P & Abbott LF (2003). *Theoretical Neuroscience: computational and mathematical modeling of neural systems*. MIT press, Cambridge.

Ecker AS, Berens P, Cotton RJ, Subramaniyan M, Denfield GH, Cadwell CR, Smirnakis SM, Bethge M & Tolias AS (2014). State dependence of noise correlations in macaque primary visual cortex. *Neuron* **82**, 235-248.

Eiber CD, Rahman AS, Pietersen ANJ, Zeater N, Dreher B, Solomon SG & Martin PR (2018). Receptive Field Properties of Koniocellular On/Off Neurons in the Lateral Geniculate Nucleus of Marmoset Monkeys. *J Neurosci* **38**, 10384-10398.

Fox MD & Raichle ME (2007). Spontaneous fluctuations in brain activity observed with functional magnetic resonance imaging. *Nat Rev Neurosci* **8**, 700-711.

Gilden DL, Thornton T & Mallon MW (1995). 1/f noise in human cognition. *Science* **267**, 1837-1839.

Goris RL, Movshon JA & Simoncelli EP (2014). Partitioning neuronal variability. *Nat Neurosci* **17**, 858-865.

Grundy D (2015). Principles and standards for reporting animal experiments in The Journal of Physiology and Experimental Physiology. *Exp Physiol* **100**, 755–758.

Hardstone R, Poil SS, Schiavone G, Jansen R, Nikulin VV, Mansvelder HD, & Linkenkaer-Hansen K (2012). Detrended fluctuation analysis: a scale-free view on neuronal oscillations. *Frontiers in physiology*, **3**, 450.

Hendry SHC & Yoshioka T (1994). A neurochemically distinct third channel in the macaque dorsal lateral geniculate nucleus. *Science* **264**, 575-577.

Hesselmann G, Kell CA, Eger E & Kleinschmidt A (2008). Spontaneous local variations in ongoing neural activity bias perceptual decisions. *Proc Natl Acad Sci USA* **105**, 10984-10989.

Jones EG (2001). The thalamic matrix and thalamocortical synchrony. *Trends Neurosci* **24**, 595-601.

Kells PA, Gautam SH, Fakhraei L, Li J, & Shew WL (2019). Strong neuron-to-body coupling implies weak neuron-to-neuron coupling in motor cortex. *Nature communications*, **10**, 1575.

27

Lee BB, Martin PR & Grünert U (2010). Retinal connectivity and primate vision (review). *Prog Ret Eye Res* **29**, 622-639.

Linkenkaer-Hansen K, Nikouline VV, Palva JM, & Ilmoniemi RJ (2001). Long-range temporal correlations and scaling behavior in human brain oscillations. *J Neurosci*, **21**, 1370-1377.

Lowen SB, Ozaki T, Kaplan E, Saleh BE & Teich MC (2001). Fractal features of dark, maintained, and driven neural discharges in the cat visual system. *Methods* **24**, 377-394.

Lowen SB & Teich MC (1996). The periodogram and Allan variance reveal fractal exponents greater than unity in auditory-nerve spike trains. *Journal of the Acoustic Society of America* **99**, 3585-3591.

Mandelbrot BB (1982). *The Fractal Geometry of Nature*. WH Freeman, New York.

Martin PR, White AJR, Goodchild AK, Wilder HD & Sefton AE (1997). Evidence that blue-on cells are part of the third geniculocortical pathway in primates. *Eur J Neurosci* **9**, 1536-1541.

McDonald JS, Clifford CW, Solomon SS, Chen SC & Solomon SG (2014). Integration and segregation of multiple motion signals by neurons in area MT of primate. *J Neurophysiol* **111**, 369-378.

Melsa JL & Sage AP (1973). *An introduction to probability and stochastic processes*. Prentice Hall, New Jersey.

Movshon JA & Newsome WT (1996). Visual response properties of striate cortical neurons projecting to area MT in macaque monkeys. *J Neurosci* **16**, 7733-7741.

Munn B & Gong P (2018). Critical Dynamics of Natural Time-Varying Images. *Phys Rev Lett* **121**, 058101.

Murray JD, Bernacchia A, Freedman DJ, Romo R, Wallis JD, Cai X, Padoa-Schioppa C, Pasternak T, Seo H, Lee D & Wang XJ (2014). A hierarchy of intrinsic timescales across primate cortex. *Nat Neurosci* **17**, 1661-1663.

Nassi JJ & Callaway EM (2009). Parallel processing strategies of the primate visual system. *Nat Rev Neurosci* **10**, 360-372.

Okun M, Steinmetz N, Cossell L, Iacaruso MF, Ko H, Barthó P, Moore T, Hofer SB, Mrsic-Flogel TD, Carandini M & Harris KD (2015). Diverse coupling of neurons to populations in sensory cortex. *Nature* **521**, 511-515.

Olshausen BA & Field DJ (1997). Sparse coding with an overcomplete basis set: a strategy employed by V1? *Vision Res* **37**, 3311-3325.

Poli D, Pastore VP & Massobrio P (2015). Functional connectivity in in vitro neuronal assemblies. *Front Neural Circ* **9**, 57.

Renart A, de la Rocha J, Bartho P, Hollender L, Parga N, Reyes A & Harris KD (2010). The asynchronous state in cortical circuits. *Science* **327**, 587-590.

Ruderman DL & Bialek W(1994). Statistics of natural images: Scaling in the woods. *Phys Rev Lett* **73**, 814-817.

Schwartz GW (1978). Estimating the dimensions of a model. *Ann Stat* **6**, 461-464.

Shine JM (2019). Neuromodulatory Influences on Integration and Segregation in the Brain. *Trends Cogn Sci* **23**, 572-583.

Sincich LC, Park KF, Wohlgemuth MJ & Horton JC (2004). Bypassing V1: a direct geniculate input to area MT. *Nat Neurosci* **7**, 1123-1128.

Smith MA & Kohn A (2008). Spatial and temporal scales of neuronal correlation in primary visual cortex. *J Neurosci* **28**, 12591-12603.

Softky WR & Koch C (1993). The highly irregular firing of cortical cells is inconsistent with temporal integration of random EPSPs. *J Neurosci* **13**, 334-350.

Solomon SS, Chen SC, Morley JW & Solomon SG (2015). Local and Global Correlations between Neurons in the Middle Temporal Area of Primate Visual Cortex. *Cereb Cortex* **25**, 3182-3196.

Solomon SS, Tailby C, Gharaei S, Camp AJ, Bourne JA & Solomon SG (2011). Visual motion integration by neurons in the middle temporal area of a New World monkey, the marmoset. *J Physiol* **589**, 5741-5758.

Tailby C, Solomon SG, Dhruv NT, Majaj NJ, Sokol SH & Lennie P (2007). A new code for contrast in the primate visual pathway. *J Neurosci* **27**, 3904-3909.

29

Tailby C, Solomon SG & Lennie P (2008a). Functional asymmetries in visual pathways carrying S-cone signals in macaque. *J Neurosci* **28**, 4078-4087.

Tailby C, Szmajda BA, Buzás P, Lee BB & Martin PR (2008b). Transmission of blue (S) cone signals through the primate lateral geniculate nucleus. *J Physiol* **586**, 5947-5967.

Teich MC (1989). Fractal character of the auditory neural spike train. *IEEE Trans Biomed Eng* **36**, 150-160.

Teich MC, Heneghan C, Lowen SB, Ozaki T & Kaplan E (1997). Fractal character of the neural spike train in the visual system of the cat. *J Opt Soc Am* **14**, 529-546.

Thurner S, Lowen SB, Feurstein MC, Heneghan C, Feichtinger HG & Teich MC (1997). Analysis, synthesis, and estimation of fractal-rate stochastic point processes. *Fractals* **5**, 565-595.

Tolhurst DJ & Thompson ID (1981). On the variety of spatial frequency selectivities shown by neurons in area 17 of the cat. *Proc R Soc Lond Ser B Biol Sci* **213**, 183-199.

Townsend RG, Solomon SS, Chen SC, Pietersen AN, Martin PR, Solomon SG & Gong P (2015). Emergence of complex wave patterns in primate cerebral cortex. *J Neurosci* **35**, 4657-4662.

van den Heuvel MP & Sporns O (2011). Rich-club organization of the human connectome. *J Neurosci* **31**, 15775-15786.

Victor JD, Blessing EM, Forte J, Buzás P & Martin PR (2007). Response variability of marmoset parvocellular neurons. *J Physiol* **579**, 29-51.

Warner CE, Goldshmit Y & Bourne JA (2010). Retinal afferents synapse with relay cells targeting the middle temporal area in the pulvinar and lateral geniculate nuclei. *Front Neuroanat* **4**, 8/1 - 8/16.

Weron R (2002). Estimating long-range dependence: finite sample properties and confidence intervals. *Physica A: Stat Mech App*, **312**, 285-299.

Xu X, Ichida J, Shostak Y, Bonds AB & Casagrande VA (2002). Are primate lateral geniculate nucleus (LGN) cells really sensitive to orientation or direction? *Visual Neurosci* **19**, 97-108.

Zeater N, Buzás P, Dreher B, Grünert U & Martin PR (2019). Projections of three subcortical visual centres to marmoset lateral geniculate nucleus. *J Comp Neurol* **527**, 535-545.

30

Zeater N, Cheong SK, Solomon SG, Dreher B & Martin PR (2015). Binocular visual responses in primate lateral geniculate nucleus. *Curr Biol* **25**, 3190-3195.

Table 1. Goodness-of-fit comparison

Data	Model	Bayesian information criterion (BIC) as multiple of power law model			
		K-cells	P-cells	M-cells	MT-cells
FF	POW	(1665.8)*	(83.2)	(129.3)	(1415.2)
		1.00	1.00	1.00	1.00
FF	EXP	1.33	3.11	1.79	1.62
FF	LOG	2.00	8.33	4.54	1.58
PS	POW	(1923.3)	(885.7)	(1126.7)	(603.0)
		1.00	1.00	1.00	1.00
PS	EXP	1.10	1.05	1.01	1.04
PS	LNM	1.27	1.48	1.24	1.07
RR	POW	(34.8)	(-152.1)	(-109.5)	(-13.0)
		1.00	1.00	1.00	1.00
RR	EXP	5.66	1.73	1.74	1.69
RR	LOG	1.47	1.10	1.02	2.6

*Absolute BIC values shown in parentheses. Abbreviations: FF, Fano-factor time curve; POW, power-law; EXP, exponential; LOG, logarithmic; PS, power spectrum; RR, rescaled-range.

31

Figure legends

Figure 1. Cell classification in LGN recordings. *A*, schematic drawing of a coronal section through the LGN. Parvocellular (P, light grey), magnocellular (M, dark grey) and koniocellular layers (K, white) are shown. Coloured points show reconstructed positions of cells recorded at a single array location. Light grey lines indicate the single cells with responses shown in B–D. *B*, peri-stimulus time histograms (PSTHs) of responses of one P on-centre (P-on) cell to a 200 ms contrast pulse. Responses to contrast increments and decrements are respectively shown as upwards– and downwards-facing PSTHs. Pulse duration is indicated by the horizontal bar between each pair of PSTHs. Cone modulation direction is indicated at the right of each PSTH. Responses to middle/long-wavelength cone modulation (ML+/-) are shown in the left column; responses to short-wave cone modulation (S+/-) are shown in the right column. *C*, *D*, responses of two koniocellular blue-on (K-bon) cells shown in the same format as B.

32
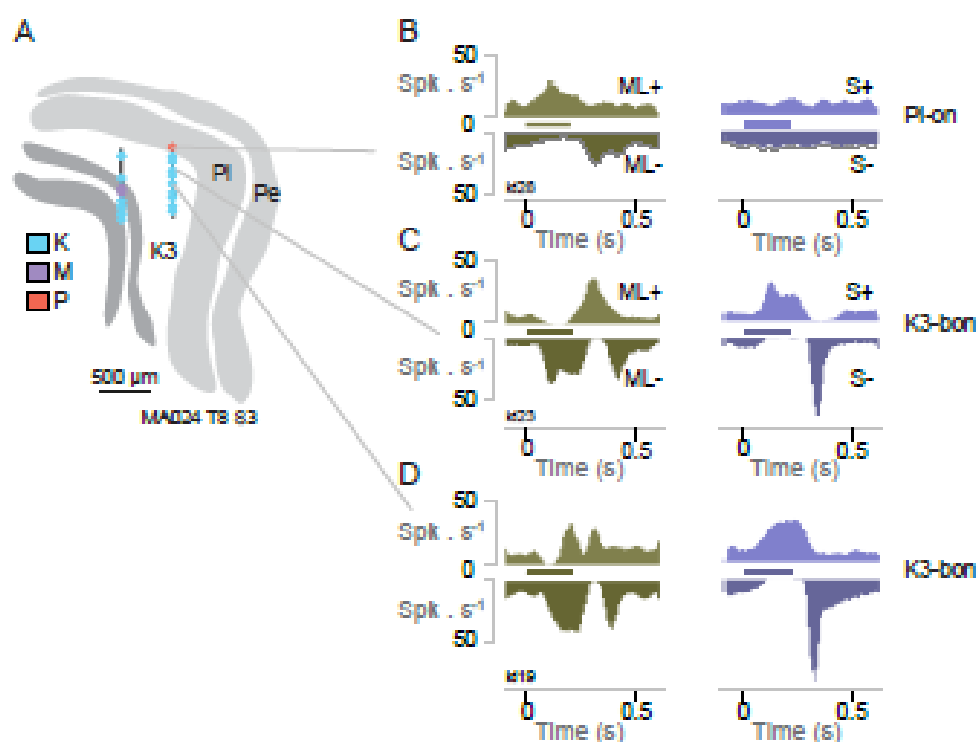
Figure 2. Fractal character of spiking. *A*, mean spike rate as a function of spike count variance in a ten second window for all recorded MT and LGN cells (K, M and P). Solid diagonal line shows Poisson (mean = variance) prediction. *B*, spike times as a function of spike index (spike number) for the three cells shown in Fig. 1 B-D. Cells were simultaneously recorded in absence of patterned visual stimulus. Linear regression for expected values of the spike index if there was no variability in spike timing is indicated for each cell as a dashed line. *C*, spike-index residuals (deviation from the linear regression calculated in B) for the cells shown in B. Note the coherent fluctuations in spike timing of the K-cells compared to the steady rate of the P cell. *D*, spike residuals calculated for another K-cell over a period of 1000 seconds (top left) with successive snapshots of the residuals in decreasing time windows to 1 second (bottom right). Note the "slow-up, rapid-down" sawtooth pattern present at multiple temporal scales.
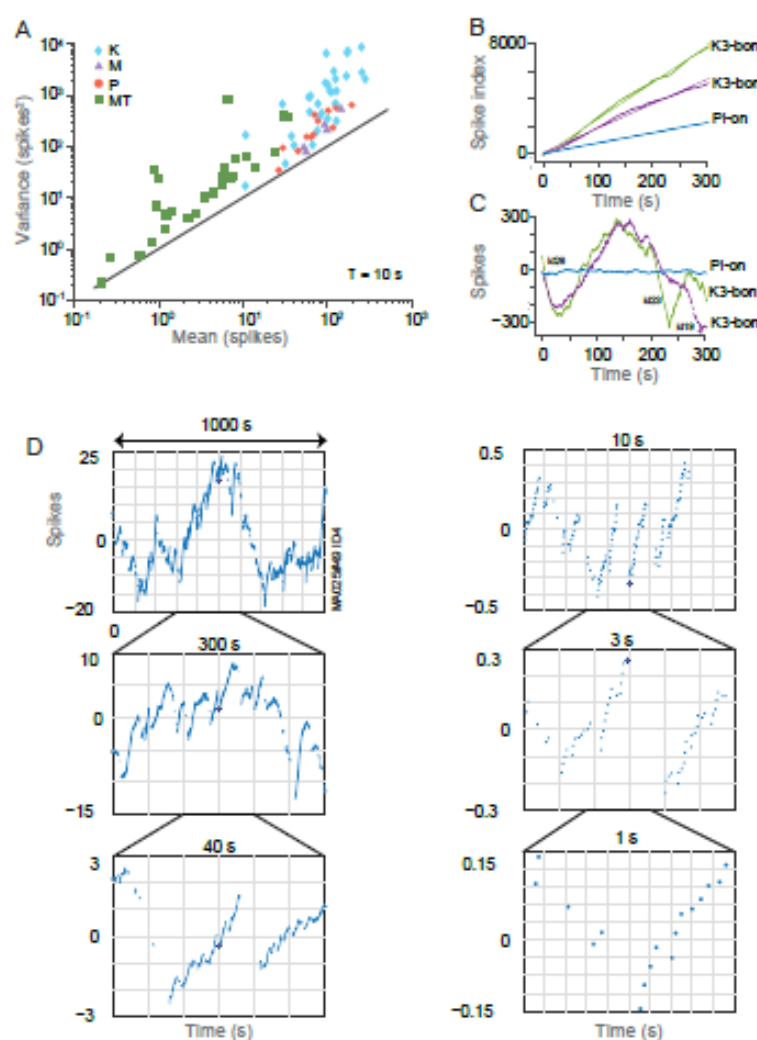
Figure 3. Fano-factor time curves. *A*, K-cells. Thick blue line shows mean value. Curves for individual cells are shown in light grey. Dark grey line shows the mean values after inter-spike intervals were shuffled. Dashed line indicates the slope of the mean Fano-factor time curve in the region where the curve follows a power law. *B*, M-cells in same format as A. *C*, P-cells in same format as A. *D*, MT-cells in same format as A. *E*, mean Fano-factor time curve ±SEM from A-D overlaid. Arrows indicate the Fano-factor window width (τ) at which each cell class diverges from Poisson-like activity and begins to follow a power-law. *F*, log-log plots of the mean power spectra of K, M, P and MT cells. The mean power spectrum for shuffled ISIs is given by the grey line. The power-law fit to the K, M/P and MT spectra are shown by dashed lines. Error bars show ±SEM.
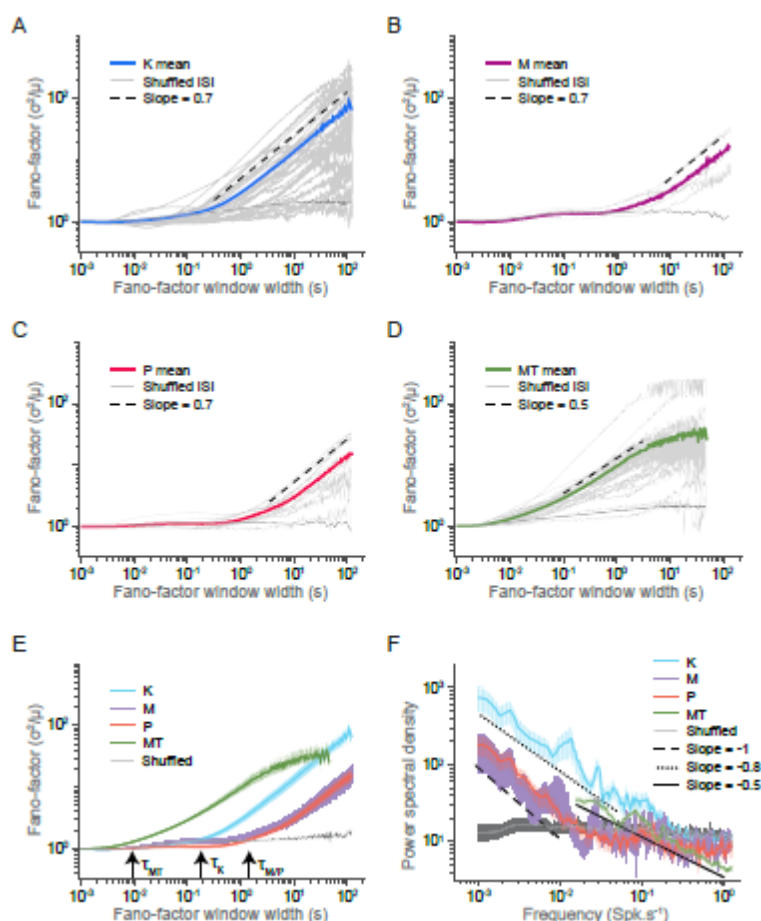
Figure 4. Rescaled range analysis of spike rates. **A**, *left column*, rescaled range (R/σ) vs. window length (τ) of an example P cell (dots). The resulting Hurst exponent *H* is calculated as the slope of the fitted line (black). *Centre column*, spike rate across the recording epoch. *Right column*, Histogram of Hurst exponents for all recorded P cells. **B-D**, same as in **A**, for M, K, and MT cells, respectively.
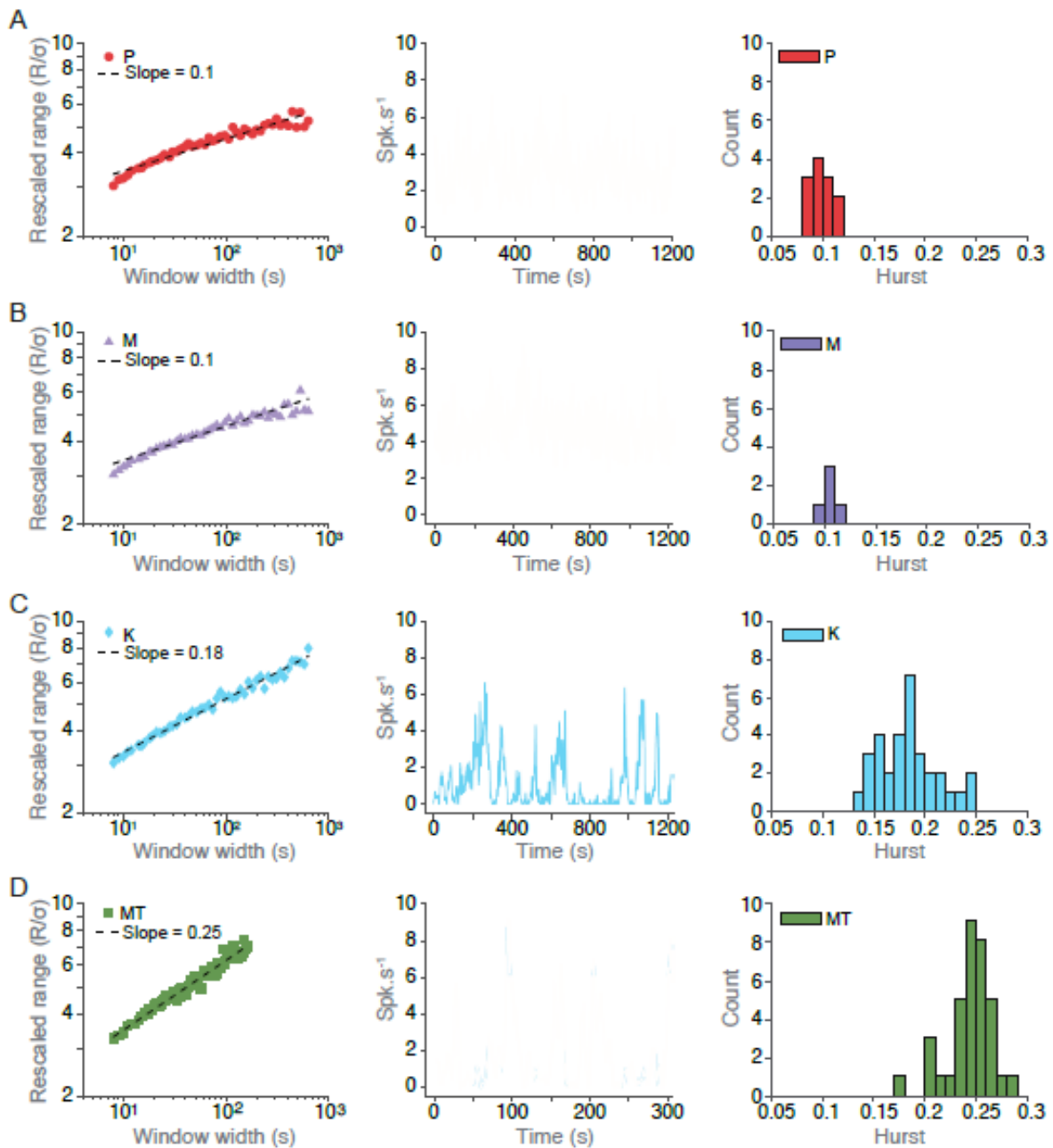
Figure 5. Population coupling analysis. ***A***, spike triggered population rate (stPR) traces from example P, M and K cells. ***B***, frequency histograms of population coupling for all recorded P, M and K cells as well as shuffled data, at zero time-lag. ***C***, scatter plots of the Fano-factor in a 10 second time window as a function of the normalised pc. ***D-F***, same analysis as in A-C, for MT cells.
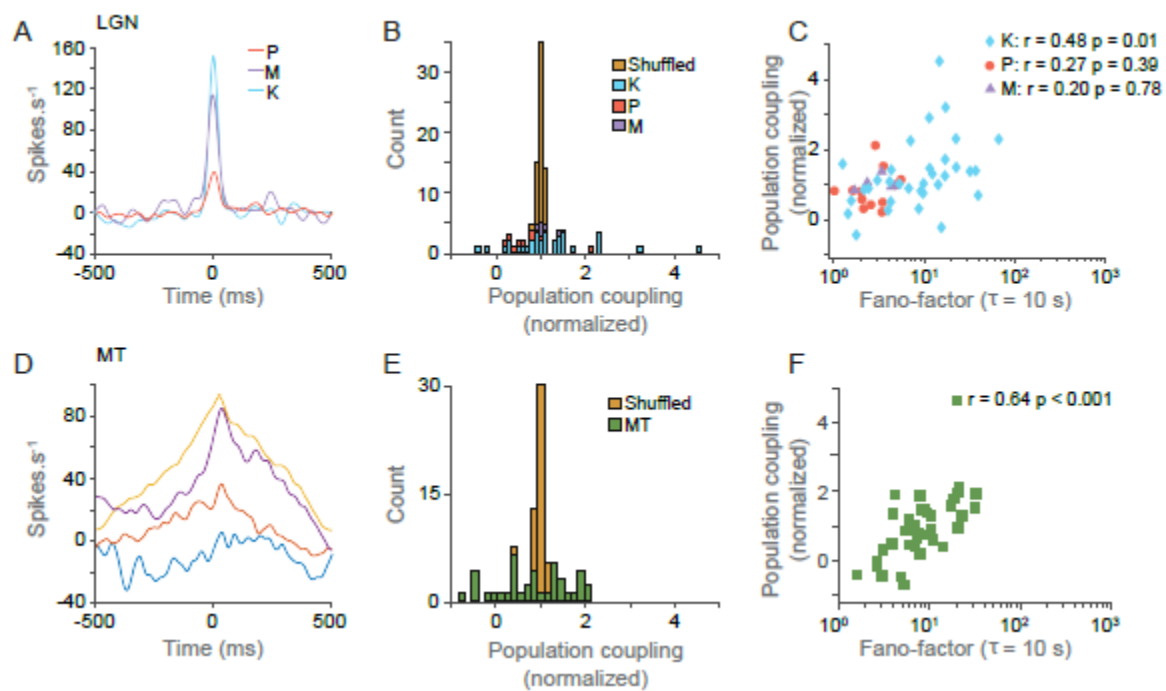
Figure 6. Noise correlation analysis. *A*, frequency histogram of noise correlations (*r*) between pairs of P, M and K cells in LGN. *B*, distribution of correlations between pairs of LGN cells as function of distance (μm) between the pairs. *C*, an example of a functional connectivity map for a single LGN recording site. Coloured points indicate isolated single cells on the recording array. Coloured lines indicate the strength of correlation between pairs of cells. *D*, higher magnification of the multiple connections of four cells from C. The chosen cell is indicated with an asterisk. *E*, scatter plot of degree of connectedness as a function of pc for cells from the two recording sites with the largest number of isolated cells. Red line shows linear regression. *F*, scatter plot of the degree of connectedness as a function of Fano-factor at time a 10 second time window from the same two recording sites as E.
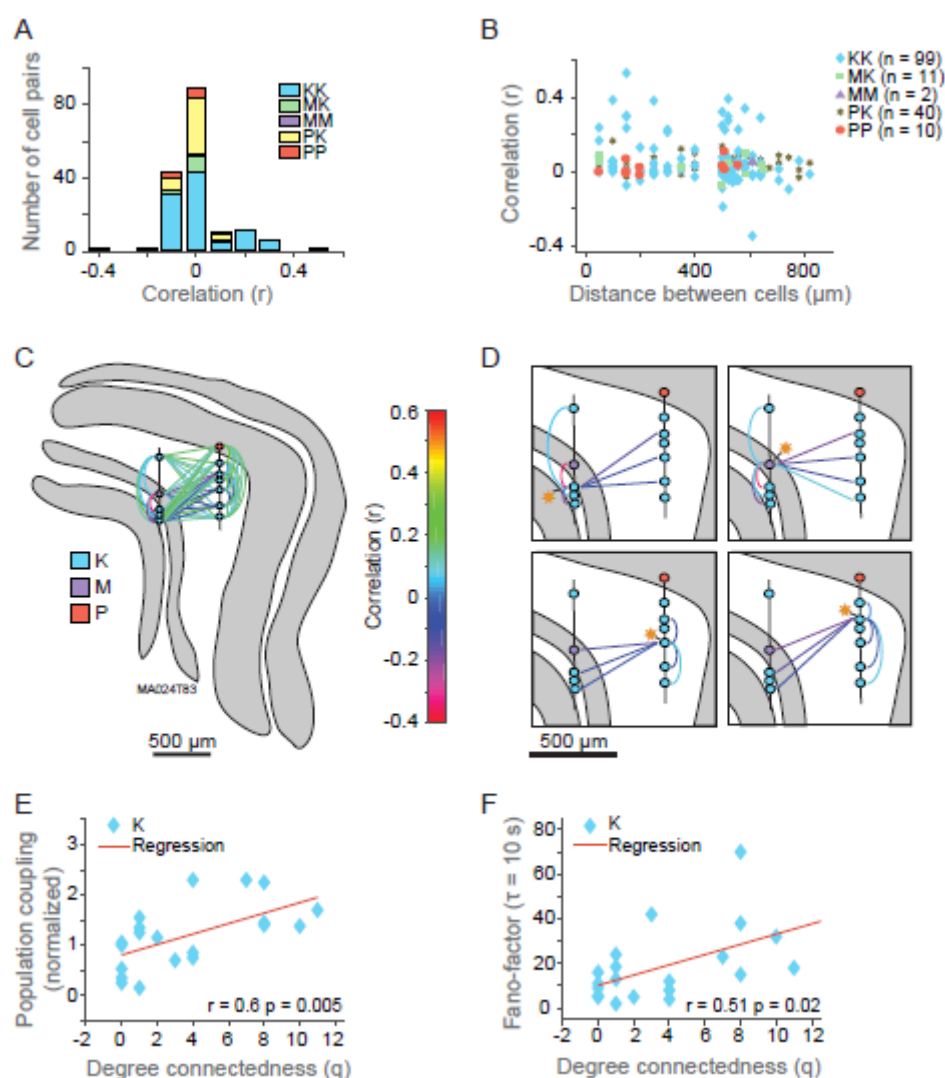
Accepted Article

Figure 7. Comparison of spike-rate (Left column) and Fano-factor time curve (right column) for various inhomogeneous Poisson processes. *A,* simulated spike rate undergoing fractal Brownian motion and Fano-factor time curves for 20 simulated cells (dark grey) and the mean Fano-factor time curve ±SEM error-bars. *B, C, D,* same as *A* for an intrinsic rate undergoing Brownian motion, 1/30 Hz oscillation, and a rate sampled from a lognormal distribution.
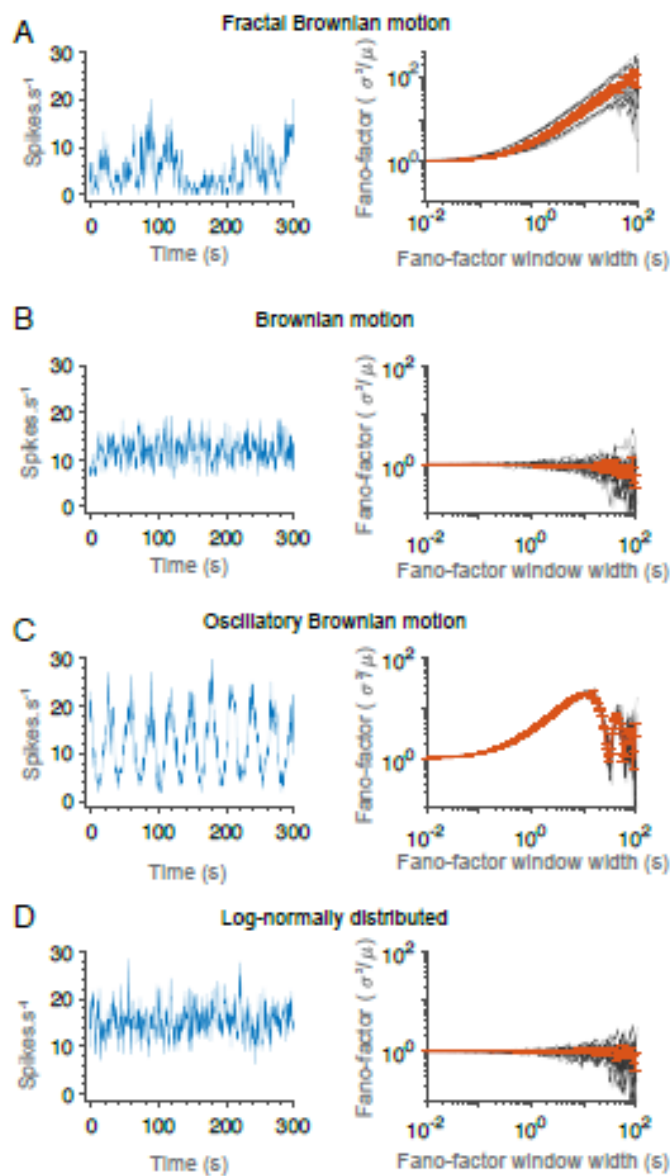

38

Figure 8. A fractal Poisson process with global gain modulation reproduces properties of empirically recorded activity. *A,* Each row shows a different cell type. Left column shows simulated spike rates. Right column shows example recordings. *B,* Each row shows a different cell population. Left column shows the pooled distribution of ISIs. Left column shows simulated data. Right column shows empirical data. *C,* mean spike rate as a function of spike count variance in a ten second window for all simulated P/M-cells (purple circles), K-cells (blue diamonds), and MT-cells (green squares). *D,* Fano-factor time curves of individual neurons (faint lines) and population mean (dark line, vertical bars are SEM) for simulated MT-cells (green), K-cells (blue), and P/M-cells (purple). Shuffling ISIs of the simulated neurons destroys the fractal relationship (grey line).
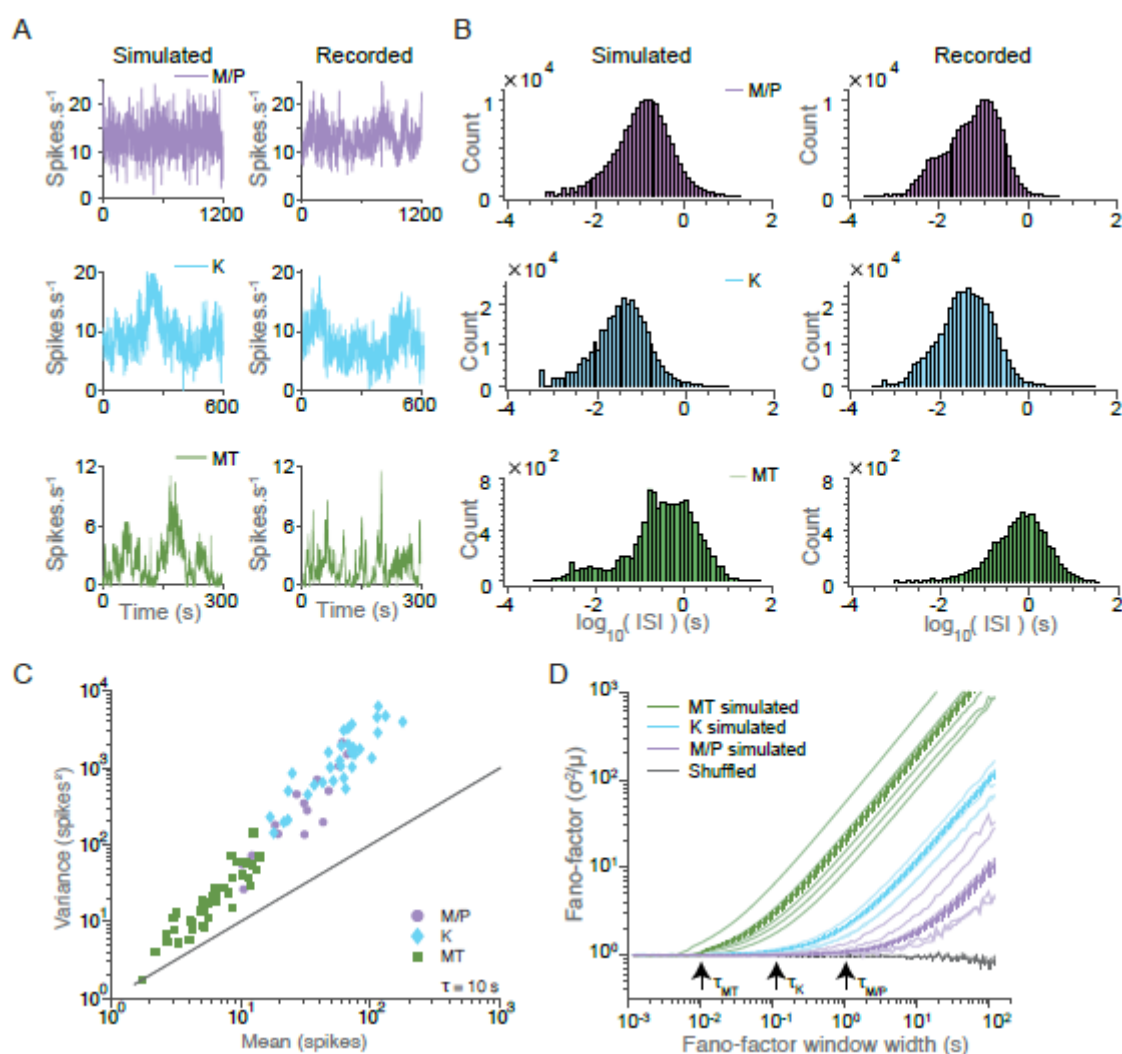
Figure 9. Effect of global modulation on normalized population coupling. ***A***, without global modulation ($G_\sigma = 0$ Hz). Left column shows stPR traces from five example simulated cells. Right column shows the normalized population coupling (pc) is very broadly distributed before (red) as the simulated cells are uncorrelated and tightly distributed after shuffling (blue). ***B***, strong global modulatory variability ($G_\sigma = 10$ Hz). Left column shows stPR traces from five example simulated cells. Right column shows the distribution of normalized pc before (blue) and after shuffling (red) is tightly distributed around unity. ***C***, intermediate global modulatory variability ($G_\sigma = 2$ Hz). Left column shows stPR traces from five example simulated cells. Right column shows the normalized pc distribution resembles the experimentally observed distribution (cf. Fig. 5B), and spike-pair shuffling reduces sharply the range of pc values.
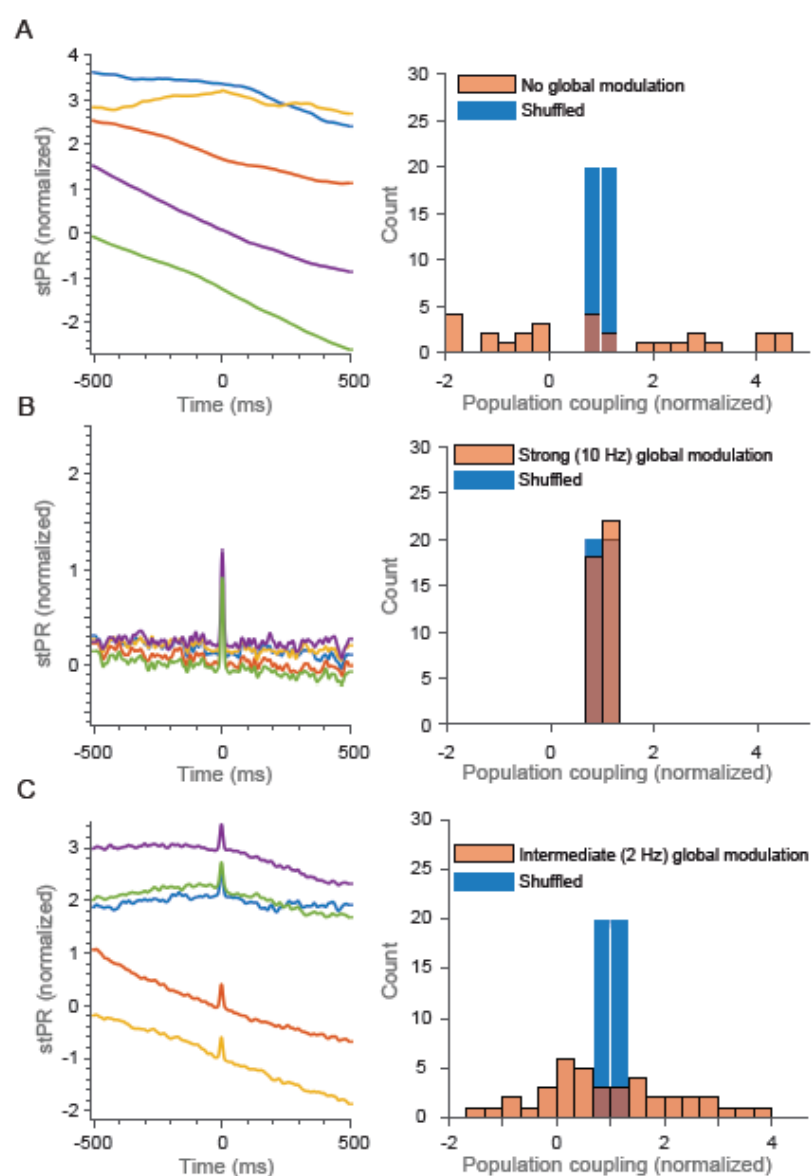
Figure 10. Relation of Fano-factor to population coupling can be explained by variability in the Hurst exponent demonstrated in 400 simulated K-cells. **A**, the model reproduces the observed positive correlation between Fano-factor ($\tau = 10$ s) and population coupling (solid red line). **B,** the population coupling of a simulated cell is positively correlated with its Hurst exponent (solid red line). **C,** the Fano-factor ($\tau = 10$ s) of a simulated cell is positively correlated with its Hurst exponent (solid red line).
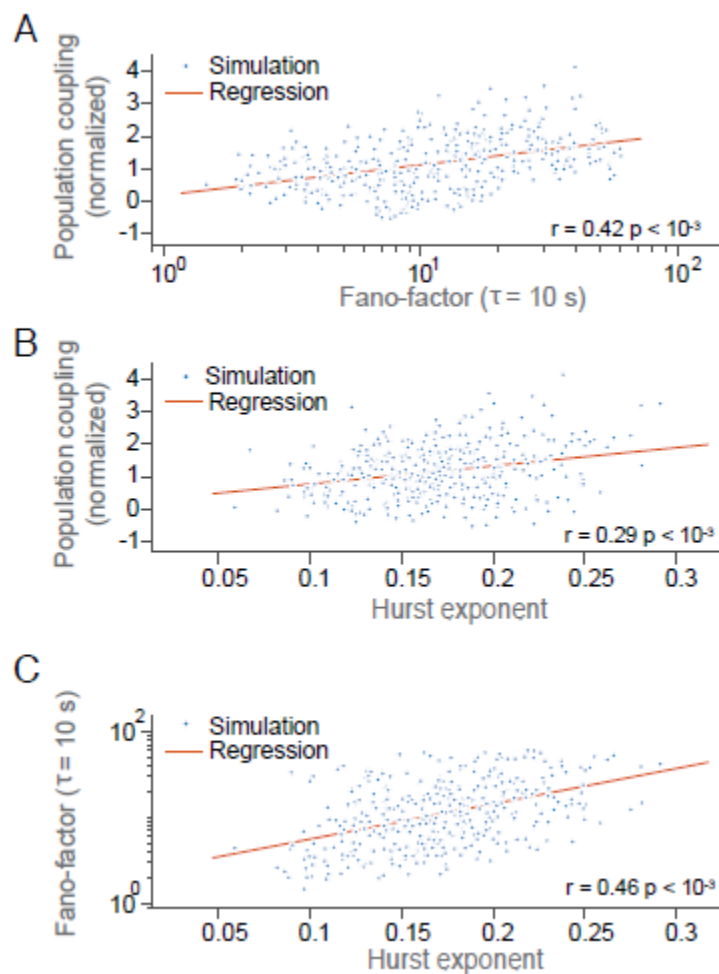
Brandon Munn

Brandon Munn received his PhD in Physics from the University of Sydney in 2019, and he is currently employed as a postdoctoral researcher at the University of Sydney, Brain and Mind Centre. His PhD research investigated mesoscale dynamics, within the early visual system. His interests are in utilising Physics methodology with a particular interest in criticality and how the brain has evolved to decode the statistics of natural scenes optimally.

Accepted Article

Natalie Zeater

Natalie Zeater received her PhD from the faculty of Medicine at the University of Sydney in 2016. She is currently a post-doc in the Save Sight Institute at the University of Sydney. Her research involves using single cell extracellular recording and immunohistochemical analysis to study the subcortical networks underlying vision.

Accepted Article